Journal of Materials Chemistry A

ROYAL SOCIETY OF CHEMISTRY

REVIEW

View Article Online
View Journal | View Issue

Cite this: J. Mater. Chem. A, 2023, 11, 18561

PEDOT:PSS materials for optoelectronics, thermoelectrics, and flexible and stretchable electronics

Xi Fan, [a] Nathan E. Stott, [a] Jixi Zeng,[a] Yunfei Li,[a] Jianyong Ouyang, *[b] Liang Chu[e] and Weijie Song *[acd]

Poly(3,4-ethylenedioxythiophene):poly(styrenesulfonate) (PEDOT:PSS) materials have emerged as promising metallic conductors and semiconductors in photovoltaics, light-emitting diodes, thermoelectrics, photodetectors and strain sensors. PEDOT:PSS serves as flexible transparent electrodes, hole transporting/injection layers, thermoelectric layers, perovskite hybrid components, motion- and temperature sensors and stretchable conductors, and it remains the research frontiers of the modern electronics. This review first introduces the basic principles of the functionalized films and their current research status. It illustrates the approaches to raise the optoelectrical and thermoelectrical properties, work function, stretchability, stability and wettability of the films. Then, the cutting-edge progresses on the aforementioned devices are highlighted. The underlying mechanism of device performance enhancements are illustrated. Besides, striking advantages but plausible issues are also pointed out. Finally, perspectives, challenges and suggestions are put forward to promote a true implementation of the optoelectronics and thermoelectrics. This featured review raises the awareness of the importance of the relationships between PEDOT:PSS properties and device performances. It guides the continued developments of the modern electronics.

Received 31st May 2023
Accepted 16th August 2023

DOI: 10.1039/d3ta03213b

rsc.li/materials-a

[a]Ningbo Institute of Materials Technology and Engineering, Chinese Academy of Sciences, Ningbo, 315201, P.R. China. E-mail: weijiesong@nimte.ac.cn
[b]Department of Materials Science and Engineering, National University of Singapore, Singapore 117574, Singapore. E-mail: mseoj@nus.edu.sg
[c]Center of Materials Science and Optoelectronics Engineering, University of Chinese Academy of Sciences, Beijing 100049, P.R. China
[d]Research Center for Sensing Materials and Devices, Zhejiang Lab, Hangzhou, Zhejiang 311121, P.R. China
[e]Institute of Carbon Neutrality and New Energy & College of Electronics and Information, Hangzhou Dianzi University, Hangzhou, 310018, P.R. China

Dr. Xi Fan obtained his PhD degree in condensed matter physics from Wuhan University in 2013. Then, he was a post-doctoral researcher at The Hong Kong Polytechnic University from 2015 to 2017, and in 2017 he was promoted to Associate Professor at Ningbo Institute of Materials Technology and Engineering, Chinese Academy of Sciences (CAS). Since 2014, his research interests had focused on the PEDOT:PSS modifications and its broad applications in photovoltaic cells, light-emitting diodes, strain sensors, and flexible and stretchable electronics.

Prof. Ouyang received his PhD, master and bachelor degrees from Institute for Molecular Science in Japan, Institute of Chemistry of CAS, and Tsinghua University in Beijing, respectively. His research interests include energy materials and devices. He invented the first polymer/nanoparticle memristor (2004), the first hybrid ionic/electronic thermoelectric converter (2020), the first adhesive intrinsically conducting polymers (2020), demonstrated the first food-processing monitors/strain sensors (2021), observed the ductilization of polymers for the first time (2022), and reported world-record conductivities and thermoelectric properties of conducting polymers and world-record thermoelectric properties of ionic conductors.

1. Introduction

Efficient photoelectric and thermoelectric energy conversions with flexibility and stretchability merits are driving the modern electronics. To maintain a competitive advantage in the electronic market, it is essential to produce a conductive and semiconductive material for the electronic integration. Poly(3,4-ethylenedioxythiophene):poly(styrenesulfonate) (PEDOT:PSS) is a classic electrically conducting polymer (CP) that has the fascinating merits of superior opt-electrical properties of metals or semiconductors, adjustable work function, high thermoelectric properties, good mechanical flexibility and stretchability, high thermal stability, and aqueous solution-manufacturing.[1–10] PEDOT:PSS is regarded as the most successful CP which has been very widely applied in the fields of photovoltaics (PVs), displays, thermoelectrics, touch sensors, and flexible and stretchable electronics.[11–20] These fields give rise to considerable demands of organic solar cells (OSCs),[21–28] perovskite solar cells (PSCs),[29–34] perovskite photodetectors (PPDs),[35–40] light-emitting diodes (LEDs),[41–48] polymer-type thermoelectrics (TEs),[47–53] intelligent robotics and health monitors,[54–58] transistors,[59–65] and so on. In these modern electronics, this CP material can serve as flexible transparent electrodes (FTEs), hole transporting layers (HTLs), hybrids with perovskites, hole injection layers (HILs), thermoelectric layers, motion and temperature sensors, electroactive layers, and stretchable conductors. In the past 20 years, Ouyang *et al.* have made plenty of pioneer works regarding doping treatments of the PEDOT:PSS and polystyrene for high optical-, electrical-, thermoelectrical- and mechanical-properties.[66–90] Since 2012, Fan *et al.* have devoted much effort to high-quality depositions of the PEDOT:PSS and MoO_3 HTLs and chemical modifications of the PEDOT:PSS electrodes for high electrical conductivity (σ), large elongation, high work function (φ), high sensitivity to tensile strain (ε), and promoted electrical and electrochemical stabilities.[91–110] As a result, memory devices, fully solution-processed flexible OSCs, stable inverted PSCs, stable colloidal quantum-dot LEDs, polymeric TEs, and plastic and durable strain sensors were subsequently realized; and new concepts of these unprecedented devices were proposed as well.[66–110]

Prof. Weijie Song received his BSc and PhD degrees from Tsinghua University, China, in 1997 and 2002, respectively. He is a professor at Ningbo Institute of Material Technology and Engineering, Chinese Academy of Science. His current research interests focus mainly on flexible optoelectronic materials and devices.

Table 1 Characteristics of Clevios and Orgacon™ PEDOT:PSS aqueous solutions, PEDOT dispersions and the films for a broad application

Product	Solid content (wt%)	PEDOT:PSS ratio (w/w)	PH (20 °C)	Particle size (nm)	Viscosity (cP)	Resistance	φ (eV)	Primary application
Clevios PH1000	1.0–1.3	1 : 1.25	1–2	Major: 120	15–50	<0.0012 Ω cm	4.8–5.2	Electrodes; thermoelectrics
P VP AI 4083	1.3–1.7	1 : 6	1–2	Max: 80	5–12	500–500 Ω cm	5.0–5.2	HTLs; HILs
PH 500	1.0–1.3	1 : 2.5	1.5–2.5	30	8–25	0.00330 Ω cm	5.0	Electrodes
P JET	1.6–2.1	1 : 6	4–7	—	4–20	1000–15000 Ω cm	5.2	Inkjet-printed HILs
HTL Solar	1.0–1.2	—	—	—	8–30	1–10 Ω cm	—	HTLs (high wettability)
F HC Solar	1.0–1.5	—	1.0–2.0	—	—	0.002 Ω cm	4.8–5.0	Electrodes (high wettability)
HTL Solar 3 (toluene)	1.5–2.5	PEDOT dispersion	—	—	—	5–500 Ω cm	—	HTLs on perovskite layers
P VP CH 8000	2.4–3.0	1 : 20	1.0–2.0	Max: 35	2–20	1×10^4 to 3×10^5 Ω cm	5.2	HILs; LEDs
Orgacon™ ICP 1050 Agfa	1.1	1 : 2.5	<2.5	—	30–100	<100 Ω sq^{-1}, <80% visible *T*%	—	Conductive hydrogels; electrodes

A series of PEDOT:PSS aqueous solutions are developed using the product names of Clevios™ by Heraeus, Orgacon™ by Agfa, *etc.* Table 1 summarizes the product information of the commonly used types of the PEDOT:PSS dispersions along with their multifunctional applications. Among them, the chosen PEDOT:PSS aqueous solutions (Clevios™) are very widely employed to prepare flexible and stretchable electrodes (Clevios™ PH500,[104] PH510,[105,106] and PH1000 commonly used) and hole transporting/injection layers (Clevios™ P VP AI 4083, Solar, and P VP8000 (ref. 107 and 108) generally employed) in lab-size electronics. The PEDOT:PSS can be very cheap if it is produced in large scale, and the PEDOT:PSS films have emerged as flexible or stretchable transparent electrodes with a superior σ, stable HTLs or HILs with an adjustable φ, hybrid components in PPDs, active TE layers, motion- and temperature sensors with high gauge factors and broad sensing regions, which have enabled emergent and promising applications that no other materials could achieve.

As a complex composed of substituted polythiophene and polyanionic compounds, as-cast PEDOT:PSS films have high uniformity and smoothness when coated on either rigid glass or thermoplastic substrates. Upon chemically doping treatments, the PEDOT:PSS thin films exhibit a high optical transparency (T%) over 92% at λ = 550 nm with 30–40 nm thickness,[106,107] tunable electrical conductivity of 10^{-3} to 10^{3} S cm^{-1}, adjustable work function of 4.7–5.3 eV, high Seebeck coefficient (S) of $\approx$50 μV K^{-1},[48] superior mechanical flexibility and large tensile strain of at least 20%. Inspiringly, the highest electrical conductivity and maximum tensile strain of the PEDOT:PSS films has been promoted to the best of all commercial products to date, beyond 4000 S cm^{-1} and 100%, respectively.[8,94,98,99] Since much effort has been devoted to the PEDOT:PSS materials that play a key role in each modern electronic, it brings PEDOT:PSS close to practical adaptations.

Several critical reviews were published with regard to PEDOT synthesis, understanding of PEDOT:PSS properties and an integration of OSCs, PSCs or TEs.[111–118] Such reviews gave an overview of the regulations of the electrical, optoelectrical or thermoelectric properties, but there is still a much room not only for a fundamental understanding of the metallic PEDOT:PSS and semiconductors, but also for a substantial raise in the film properties (σ, φ, S, ε, sensitivity, stability, durability, wettability, *etc.*) that dominate the device performances. Furthermore, considering (i) a great universality of the modification methods of PEDOT:PSS for potentially guiding other device construction despite the different roles of the PEDOT:PSS films played in these OSCs, PSCs, PPDs, LEDs, TEs, strain sensors and flexible and stretchable electronics; (ii) fast developments and significant breakthroughs of the aforementioned electronics especially achieved in the last 4 years; and (iii) a substantial lack of a featured review that can focus on the cutting-edge methods and strategies and regulation mechanisms of the PEDOT:PSS properties, which are strictly required by the various modern electronics. Therefore, it become reasonable, emergent and critical to make a panoramic review with a specialized category introduced below.

In the review, we first present the fundamental basis on the optoelectrical-, thermoelectric-, mechanical- and wettability-properties, work function, stability as well as charge-transfer underlying mechanisms of the PEDOT:PSS materials. Then, it indeed provides a broad overview of the significant breakthroughs and most cutting-edge progresses on the modern electronics including OSCs, PSCs, PPDs, TEs, LEDs, strain sensors, and flexible and stretchable devices (Fig. 1). According

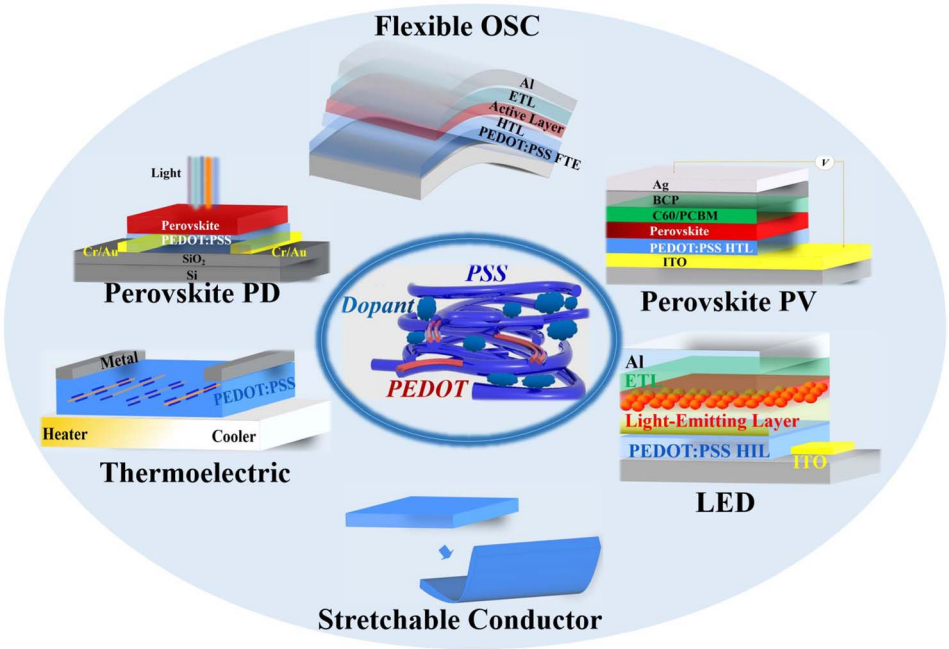

Fig. 1 Schematic diagram of PEDOT:PSS applications in various optoelectronic and thermoelectric devices discussed in the review.

to the category of each device and the key role of PEDOT:PSS which plays in each device, the sections are divided briefly into five parts: (i) cutting-edge fabrication approaches of the PEDOT:PSS electrodes used in ITO-free and flexible OSCs, (ii) modification methods of the PEDOT:PSS HTLs along with broad applications in inverted PSCs, (iii) three-type PEDOT:PSS films (*i.e.*, hybrids, HTLs and FTEs) for halide perovskite photodetectors, (iv) strategies to raise thermoelectric properties of PEDOT:PSS and its components, and (v) means to prepare conductive, stretchable and motion-sensitive PEDOT:PSS conductors for these stretchable electronics involving strain sensors, stretchable optoelectronics and thermoelectrics. All the methods to regulate the PEDOT:PSS properties are systematically summarized, directly linking them to the underlying mechanisms of the performance enhancements of the modern electronics. Finally, challenges, outlooks and suggestions on both developments of emergent PEDOT:PSS materials and as-integrated modern electronics are illustrated at the end of the review.

2. Fundamental considerations for PEDOT:PSS electrodes in OSCs

Indium tin oxide (ITO)-free and flexible OSCs have stimulated tremendous attentions during the past decade. The flexible OSCs are commonly composed of an active layer sandwiched between a transparent electrode coated with a HTL and a metal negative electrode coated with a low-work-function ETL. PEDOT:PSS is one of the most representative FTEs owing to its good conductivity, high optical transmittance, superior flexibility, high uniformity, and low roughness. Since such highly conductive PEDOT:PSS transparent electrodes were attained through using the 1.0 M sulfuric acid (H_2SO_4) treatment[73] by Ouyang *et al.* in 2012, a tremendous effort had been devoted to the polymer electrode preparation and flexible OSC construction. On the basis of an optimal PEDOT:PSS FTE, the single-junction normal flexible OSCs based on binary active layers exhibited a record-high power conversion efficiency (PCE) of 16.61% reported by Fan *et al.* in 2021.[94]

A crucial factor in FTE performances is an electrical property. The electrical property of a thin film is generally evaluated by the sheet resistance (R_{sh}) and σ using a van der Pauw four-point probe technique, $R_{sh} = \pi R/\ln 2$, $\sigma = R_{sh}/L$, where R is the voltage between AB contacts to CD contacts (A, B, C and D are the four points of a square); σ is electrical conductivity; and L is the film thickness. In order to achieve a high σ, PEDOT crystallization, phase-segregated morphology and PEDOT/PSS ratios in matrices should be considered together with respect to the electrode preparation. The PEDOT crystallization is mostly determined by a structural conformation, which means a high electrical conductivity that mostly arises from an evolution of PEDOTs from benzoid structures to quinoid structures.[119–121] A favorable phase-segregated morphology is induced by a weak coulombic attraction between PEDOT and PSS. While a low PEDOT/PSS ratio in the polymer matrices rather than only upon the surfaces demonstrates a lower sulfonate component, and it results in a high electrical conductivity because PSS is an insulating component.

In this section, we focus on the cutting-edge doping treatments and unique processing technologies that substantially raise the conductivity, work function and wettability of the PEDOT:PSS FTEs. Progresses on ITO-free flexible OSCs are highlighted briefly, and suggestions are provided for the continued developments of both CP electrodes and flexible OSCs.

2.1. Secondary doping with $HClO_4$ and CF_3SO_3H

In 2020, perchloric acid ($HClO_4$) treatments are proposed for the first time by Fan *et al.* to chemically dope the PEDOT:PSS (Clevios™ PH1000) thin films as a FTE.[99] As the strongest inorganic acid with ultrahigh acidity (p*K*a: −10) over those of H_2SO_4 (p*K*a: −3.0) and methanesulfonic acid (CH_3SO_3H, p*K*a: −1.9), the $HClO_4$ treatments can provide a strong protonation of hydrogen ions (H^+) to insulating PSS chains, thereby resulting in a high electrical conductivity. This optimal 0.1 M $HClO_4$ treatment endowed the PEDOT:PSS electrodes with $\approx 32\ \Omega\ sq^{-1}$ sheet resistance, 90.4% transmittance at $\lambda = 550$ nm, and a better wettability towards the HTL droplet. The high wettability was due to a sulfonate-rich hydrophilic component on the electrode surfaces and a unique spray-coating of $HClO_4$ ultrathin layers that bonded between the PEDOT:PSS electrodes and PEDOT:PSS (Clevios™ P VP AI 4083) HTLs. Consequently, it led to a small contacting angle (θ) of only 17° for an intimate interface contact. Besides, the $HClO_4$ molecules induced a high work function (estimated value: 5.39 eV) for the PEDOT:PSS films *via* a polarization effect, owing to the polar chlorine–oxygen bonds of $HClO_4$ with uncoupled charge centers. Therefore, a small potential barrier was induced at the interfaces through minimizing the energy level mismatch among the FTEs, HTLs and electron donors of active layers. As a result, the fully solution-processed flexible OSCs exhibited a 16.41% efficiency on the basis of a binary active layer of PM6:Y6 (Fig. 2a).

In 2021, Fan *et al.* proposed a low-temperature (50 °C) and low-concentration (0.8 M) trifluoromethanesulfonic acid (CF_3SO_3H) treatment for constructing a fully solution-processed flexible OSC (Fig. 2b).[94] CF_3SO_3H is a super acid with an ultrahigh acidity (p*K*a: −15) and it provides a strong protonation of H^+ into PSS for high conductivity and better morphology. Owing to a polarization of polar carbon–fluorine (C–F) covalent bonds of CF_3SO_3H with uncoupled charge centers, the PEDOT:PSS films had a raised work function of up to 4.99 eV. The 0.8 M CF_3SO_3H treatment at 50 °C induced a low sheet resistance of $\approx 35\ \Omega\ sq^{-1}$, a transmittance of 87.5% at $\lambda = 550$ nm, a high work function of 4.99 eV and a superior hydrophilicity with θ of 23.5°. The optimized flexible OSCs exhibited the highest PCE of 16.61% (Fig. 2b). To the best of our knowledge, 16.61% is the highest PCE for single-junction ITO-free normal flexible OSCs with binary active layers reported thus far. Notably, both $HClO_4$ and CF_3SO_3H treatments are indeed gentle and effective, consequently, the photovoltaic cells showed a high flexibility and a good thermal stability in a 200 hours thermal processing at 85 °C, *i.e.*, a decrease by 9.1% in PCE in the thermal stability test. These optimal acid recipes open a methodology to invent

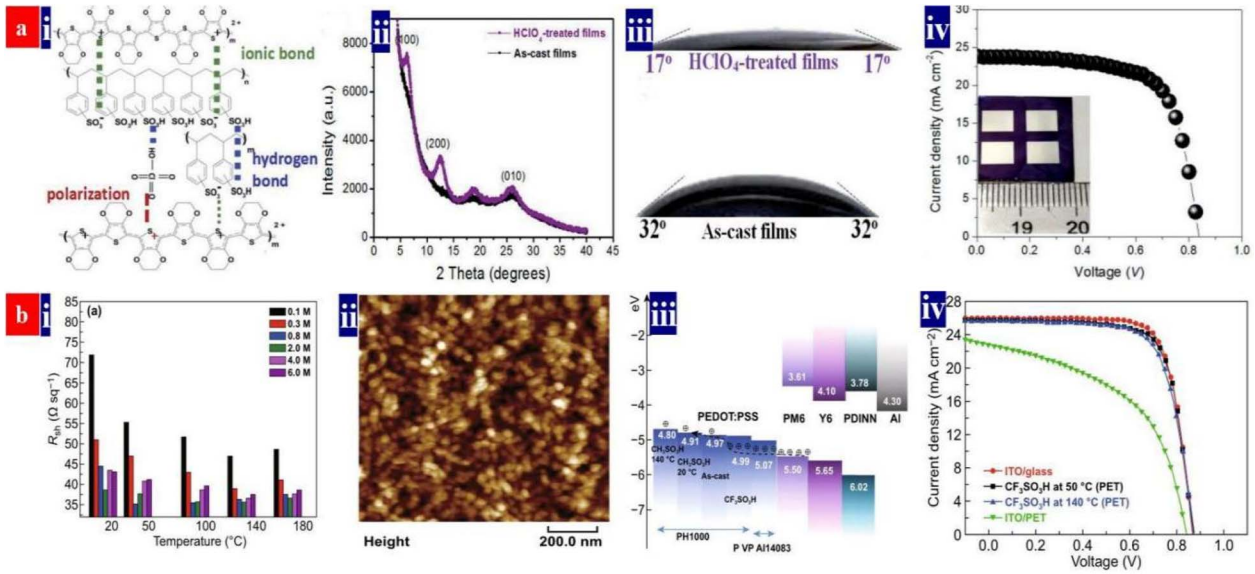

Fig. 2 (a) (i) Inter-molecular interactions among PEDOT, PSS and $HClO_4$; (ii) XRD spectra of the pristine and $HClO_4$-treated films; (iii) wettability of the droplets (P VP AI 4083) on the pristine and 0.1 M $HClO_4$-treated electrodes; and (iv) *J*–*V* characteristics of flexible OSCs with the PEDOT:PSS electrodes (active area: 0.3 cm^2). Reproduced with permission.[99] Copyright 2020, Royal Society of Chemistry. (b) (i) Sheet resistances of the PEDOT:PSS electrodes; (ii) morphology of PEDOT:PSS nanoparticles; (iii) energy levels of the device components; and (iv) *J*–*V* characteristics of flexible OSCs with PEDOT:PSS and ITO electrodes (active area: 0.04 cm^2), and the rigid OSCs fabricated on ITO/glass substrates. Reproduced with permission.[94] Copyright 2021, Springer Nature.

high-performance fully solution-processed flexible OSCs based on strong acid and super acid-treated PEDOT:PSS FTEs. Table 2 summarizes the photovoltaic characteristics of the ITO-free flexible OSCs based on PEDOT:PSS electrodes and metal electrodes reported recently.

2.2. Shearing technologies for thin film fabrication

A solution-shearing technology differs from conventional spin-coating ones and spray-coating ones, and it allows for a kinetic control over film morphology, composition and anisotropy *via* controlling the blading rate and temperatures of rigid substrates such as glass and silicon. Bao *et al.*[3] reported a PEDOT:PSS electrode deposited by solution shearing at 130 °C. The PEDOT:PSS films were deposited at 65–85 °C on a temperature-controlled shearing stage; then, the films were placed on a hotplate at 130 °C, followed by dropping methanol on PEDOT:PSS tops. The solution-sheared PEDOT:PSS films were thermally annealed, cooled to room temperature, and rinsed with methanol. The specific control over deposition conditions allows for a tunable phase separation and a preferential PEDOT backbone alignment, thereby leading to a high conductivity. The solution-sheared electrodes showed more prominent well-defined fibers which were more elongated at a faster shearing speed of 3.0 mm s^{-1}.

A local segmental chain dynamic is affected by the viscosities of polar solvents,[122] such as methanol, ethylene glycol (EG), and ethanol (EtOH). For example, the solvation of PSS is sensitive to the viscosities of the chosen polar solvents. Through adjusting the PSS solvation and structural rearrangement of PEDOT, a special shearing treatment using two solvents may induce PEDOT-rich domain ordering. On the principles, Bao *et al.*[123] proposed a solvent-shearing technology using two solvents (methanol : EtOH = 1 : 1) that resulted in a highly conductive PEDOT:PSS electrode. The solvent-sheared PEDOT:PSS films were prepared by solution shearing (90 °C and 1.5 mm s^{-1}) and subsequently treated by the sheared solvents at 90 °C in ambient air. This shearing deposition induced a larger PEDOT/PSS ratio, which was attributed to the partial removals of PSS and the improved π–π stacking of the PEDOTs.

It is suggested that all of the parameters (thickness, uniformity, sheet resistance, and figure of merit) of each solvent-sheared film should be rigorously measured for precisely estimating the electrical conductivity. A main consideration is that the manufacturing processes of solvent-sheared films are rather complicated, at least involving solution-shearing, solvent-shearing, pre- and post-thermal annealing, and submerging in solvents. Film deposition quality, uniformity and thickness are sensitive to blading parameters, evaporation rates of solutions and solvents, ambient air conditions and storage times. In addition, on the basis of these PEDOT:PSS electrodes with superior conductivity, highly efficient lab-scale photovoltaic cells should be realized. The high photovoltaic performances of the photovoltaic cells not only can verify the reproducibility of the high-merit transparent electrodes, but also exemplify the great superiority of the most cutting-edge electrode preparation methods in terms of raising the charge extraction.

2.3. Layer-by-layer doping treatments

The electrical conductivity of the PEDOT:PSS films has been enhanced by the treatments of secondary polar solvents, strong

Table 2 Photovoltaic performances of flexible OSCs with PEDOT:PSS and metal FTEs

Device structure	FTE	V_{OC} (V)	J_{SC} (mA cm^{-2})	FF	PCE	Retained (PCE)	Flexing test	Ref.	Year
PI/FTE/ZnO/PM6:N3:$PC_{71}BM$/MoO_3/Ag	Ag NW/AZO	0.84	25.0	0.765	16.1%	90%	2×10^3 cycling at r: 1.0 mm	26	2020
PET/FTE/AI4083/PM6:Y6/PNINN/Al	0.1 M $HClO_4$-treated PEDOT:PSS	0.85	25.83	0.748	16.44%	—	—	99	2020
PET/FTE/AI4083/PM6:Y6/PNINN/Al	0.8 M CF_3SO_3H-treated PEDOT:PSS	0.86	25.83	0.748	16.61%	90%	10^3 cycling at r: 1 mm	94	2021
PET/FTE/ZnO/PM6:N3:$PC_{71}BM$/MoO_3/Ag	Em-Ag/Ag NW/AZO	0.835	27.37	0.769	17.52%	90%	1.2×10^3 cycling at r: 5 mm	19	2022
PET/FTE/ZnO/PM6:Y6/MoO_3/Ag	Em-Ag/Ag NW/AZO	0.833	25.55	0.738	15.71%	—	—	19	2022
PI/Ag/PCP-Li/AI4083/PM6:Y6:$PC_{71}BM$/Bia-FIMG/FTE	10 nm-thick Ag/TeO_2	0.836	24.77	0.753	15.6%	92%	10^5 cycling at r: 4 mm	28	2022
Polyimide/FTE/AI4083/PM6:Y6/PNINO/Al	Cr	0.84	25.8	0.702	15.2%	90%	10^3 cycling at r: 3.0 mm	27	2020
PET/FTE/ZnO/PM6:Y6/MoO_3/Al	72 wt% $HClO_4$-treated PEDOT:PSS	0.85	25.83	0.748	15.03%	—	—	99	2022

acids, ionic liquids, *etc*.[37–39,73,124,125] Among these methods, a strong acid treatment has emerged as one of the most effective methods to boost the film conductivity. One reason is the large removal of insulating PSS on the surfaces of the CP films. However, it hardly made a large removal of PSS from the whole PEDOT:PSS matrices, especially from the bottom half of the matrices. As such, the PEDOT:PSS transparent electrodes tend to exhibit a limited opto-electrical trade-off with a figure of merit (FoM) of <80.[98]

A unique layer-by-layer (LBL) doping not only makes the large removals of PSS in the whole matrices rather than on the surfaces, but also induces a better phase-segregated morphology extruding large-domain aggregates. In 2020, Fan *et al.* proposed a unique LBL co-doping method that substantially improved the optical and electrical properties of the PEDOT:PSS electrodes coated on glass substrates.[98] The PEDOT:PSS electrodes exhibited a record-high FoM of ≈100, which was due to (i) the effective doping of the PEDOT:PSS matrices for a high hole concentration (7.25×10^{21} cm^{-3}) and hole mobility (3.62 cm^2 V^{-1} s^{-1}), (ii) a large removal of the insulating sulfonate components in matrices, and (iii) a refined phase-separated morphology without large-domain aggregates. On the basis of the LBL-treated PEDOT:PSS electrodes, a vacuum-free, all-solution and all-air processed OSC yielded a high PCE of 11.12%. To clearly describe the morphological evolution and structural rearrangement of the electrodes, the schematic diagrams of the models were illustrated (Fig. 3a). It explains why the LBL-treated CP electrodes have the outstanding optoelectrical properties over the conventional ones with secondary polar solvent or strong acid treatments. Generally, with the conventional strong acid treatments, the films which consist of small aggregates have many refined PEDOT-rich nanofibrils on the top half. An achievement of ordered stacking of PEDOT could be induced by the strong acid treatments.[125] After the unique LBL doping treatment, more PEDOT-rich nanofibrils are induced from the coiled deformations to the linear/extended-coil deformations. Besides, it largely reduced the insulating PSS components in the whole matrices including the front and rear sides (Fig. 3b). As a result, the CP electrodes not only yielded the record-high FoM of up to 100 along with σ of 4200 S cm^{-1}, but they also showed an enhanced electrical stability and a much better electrochemical stability under a cyclic voltammetry testing in anhydrous dichloromethane while using 0.1 M Bu_4NPF_6 as an electrolyte.

The limited electrical conductivity of PEDOT:PSS FTEs is a remaining major challenge of the PEDOT:PSS FTEs at present. Although many approaches dramatically improve the conductivity over 4000 S cm^{-1}, such a film conductivity still lags far behind the estimated values (13 000 (ref. 121) and 16 600 (ref. 91) S cm^{-1}) of the commercial ITO electrodes sputtered on glass substrates; furthermore, most of strong acid treatments reported previously were corrosive to underlying metallic nanowires and grids. Therefore, novel recipes for strong acid treatments and other acid-free doping treatments should be developed to further improve the CP conductivity and such methods need to be compatible with most of underlying thermoplastic substrates and the component transparent electrodes

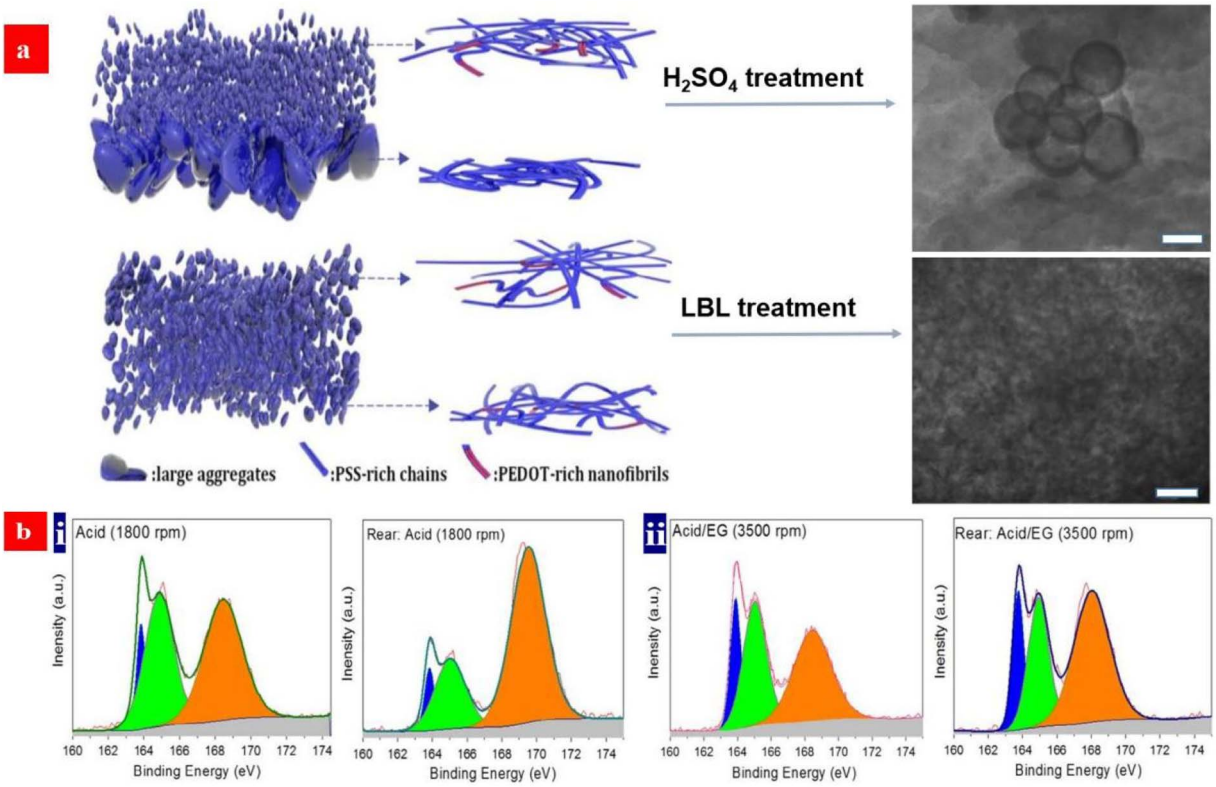

Fig. 3 (a) Schematic diagram of morphology of the acid-treated films and LBL-treated films, respectively. (b) Fitted S 2p XPS Spectra of the front and rear sides of the PEDOT:PSS films: (i) the acid-treated PEDOT:PSS films at spin coating of 1800 rpm; and (ii) the acid and EG co-treated PEDOT:PSS films at spin coating of 3500 rpm. Reproduced with permission.[98] Copyright 2020, Wiley-VCH.

that consist of the CPs and metal nanowires or grids. The improvement of the underlying mechanisms of both stability and flexibility enhancements for the photovoltaic cells should be sought in the future.

3. Fundamental considerations for PEDOT:PSS HTLs in PSCs

Perovskite solar cells have been on the forefronts of novel photovoltaics over the past decade.[126–129] The perovskites are a category of compounds with the structure of ABX_3, where A is organic cations including $CH_3NH_3^+$ (MA^+) and $HC(NH_2)_2^+$ (FA^+), B is Pb^{2+} or Sn^{2+}, and X is a halogen anion such as I^-, Br^-, and Cl^-. The perovskite layers exhibit excellent optoelectronic properties such as a wide visible light absorption spectrum, high absorption coefficient, high charge carrier mobility, low exciton binding energy, high defect tolerance, and long electron and hole diffusion length. The current champion of the PSCs exhibited an inspiring PCE as high as 26.08% (certified 25.73%) under standard illumination.[127] The single-junction PSCs have two types of structures: conventional ones and inverted ones. The conventional one involves a bottom ETL of metal-oxides such as titanium dioxide (TiO_2) and tin dioxide (SnO_2) coated onto ITO films. The inverted one involves a bottom HTL coated on ITO films, such as PEDOT:PSS, polybis(4-phenyl)(2,4,6-trimethylphenyl)amine (PTAA), and poly(3-(4-methylamincarboxylbutyl)thiophene) (P3CT-N). The inverted PSC devices have the striking advantage of negligible device hysteresis; meanwhile, the harsh sintering treatments at high temperatures can be extruded in the device fabrication.

In the inverted PSCs, a HTL should have a high work function, good wettability and suitable electrical conductivity as minimum requirements. The work function of the HTLs can be confirmed by ultraviolet photoelectron spectra (UPS), $\varphi = h\nu + E_{\text{cutoff}} - E_{\text{Fermi}}$, where E_{cutoff} and E_{Fermi} is the low kinetic energy cutoff and Fermi level, respectively. A hydrophilic PEDOT:PSS HTL facilitates the target formation of perovskite crystallinity consisting of large grains. Owing to an adjustable electrical conductivity, high work function and high solubility, the PEDOT:PSS (Clevios™ P VP AI 4083) products are the promising HTL and HIL materials used to fabricate the currently existing photovoltaics and LEDs, respectively.

A modified PEDOT:PSS film can have φ of 4.7–5.3 eV. A high φ of the HTLs allows for a formation of ohmic contacts and it is favorable for hole transport from the perovskite layers to the transparent electrodes. The work function of the CP HTLs depends on the PEDOT:sulfonate ratios, electron withdrawing groups (*e.g.*, –Cl, –F, –Br, $-SO_3^-$) of dopants, PEDOT crystallinity, *etc*. The section provides an overview of significant progresses on both modified PEDOT:PSS HTLs and inverted PSCs. Approaches to tune the properties of the PEDOT:PSS HTLs are clearly introduced. The underlying mechanisms for

enhancement of device-efficiency and some related suggestions are illustrated as well.

3.1. Sulfonate treatments

Typically, exciton quenching occurs at the interfaces between PEDOT:PSS (Clevios™ P VP AI 4083) HTLs and halide perovskite layers, and thus, it delays the device efficiency *via* a radiative recombination of charge carriers. Ding's group reported a PEDOT:PSS (P VP AI 4083) HTL that was treated by the polymer electrolyte of sodium polystyrene sulfonate (PSSNa) to improve its work function.[130] Compared to that of the pristine one, the work function of the PSSNa-treated PEDOT:PSS HTL was higher by 0.3 eV, which led to an open circuit voltage (V_{OC}) of 1.11 V and a PCE of 15.56% (Fig. 4a). Subsequently, Zang's group employed sodium benzenesulfonate ($C_6H_5SO_3Na$) to modify the PEDOT:PSS (P VP AI 4083) HTLs.[131] It led to a smooth surface of the PEDOT:PSS HTLs as well as a better energy level alignment with the perovskite crystalline layers. Besides, the $C_6H_5SO_3Na$ treatment raised the hole extraction capacity and it suppressed charge recombination, thereby increasing the grain size and crystallinity of the $MA_{0.8}FA_{0.2}PbI_{3-x}Cl_x$ perovskite films (Fig. 4b). Consequently, the PCE and V_{OC} of the inverted PSCs were improved to 19.41% and 1.08 V, respectively, which are higher than those (PCE: 18.07% and V_{OC}: 1.04 V) of the control inverted PSCs without the $C_6H_5SO_3Na$ treatment. It should be also mentioned that sulfonate treatments caused rich sulfonate components in PEDOT:PSS matrices, presumably resulting in a stability issue of the PSCs due to the strong intrinsic hygroscopicity of the sulfonate components. Therefore, a small doping content of the sulfonates is critical for an adaptation of the inverted PSCs based on the PEDOT:PSS HTLs with promoted stability against humidity and ultraviolet lights. Besides, with respect to the sulfonate treatments, other concentrations and small gradients especially between 3 and 15 mg mL^{-1} should be used for the PSC device optimization. We envision that a similar treatment using the sulfonates (*e.g.*, CF_3SO_3Na) involving electron withdrawing groups may further raise the work function and morphology of the PEDOT:PSS HTLs for a better photovoltaic cell.

3.2. Sodium- and cesium salt treatments

To illustrate the significant effect of the PEDOT:PSS HTL modifications on PSC performances, Hu *et al.*[132] reported an effective and simple treatment by adding 5 mg mL^{-1} sodium chloride (NaCl) into the PEDOT:PSS (P VP AI 4083) aqueous solutions. The PCE of the inverted PSCs based on the NaCl-doped HTLs was much higher than that of the control solar cells with the pristine PEDOT:PSS HTLs (Fig. 5a). Note that the best PSCs delivered a PCE of up to ≈18.2% with a fill factor (FF) as high as 0.800. The high PCE is attributed to two factors as follows: (i) a raised electrical conductivity and hole extraction of the NaCl-treated PEDOT:PSS HTLs and (ii) a preferred orientation along the (001) direction of the uniform perovskite films on the NaCl-treated PEDOT:PSS HTLs. Subsequently, Jiang *et al.*[133] developed a similar strategy through doping the PEDOT:PSS with cesium iodide (CsI). The CsI treatment reduced the voltage loss and it enabled a high-efficiency inverted PSC based on the PEDOT:PSS HTLs. CsI materials reacted with the PbI_2 materials. This chemical reaction not only led to a formation of $CsPbI_3$ but also induced a better interfacial contact for charge-carrier

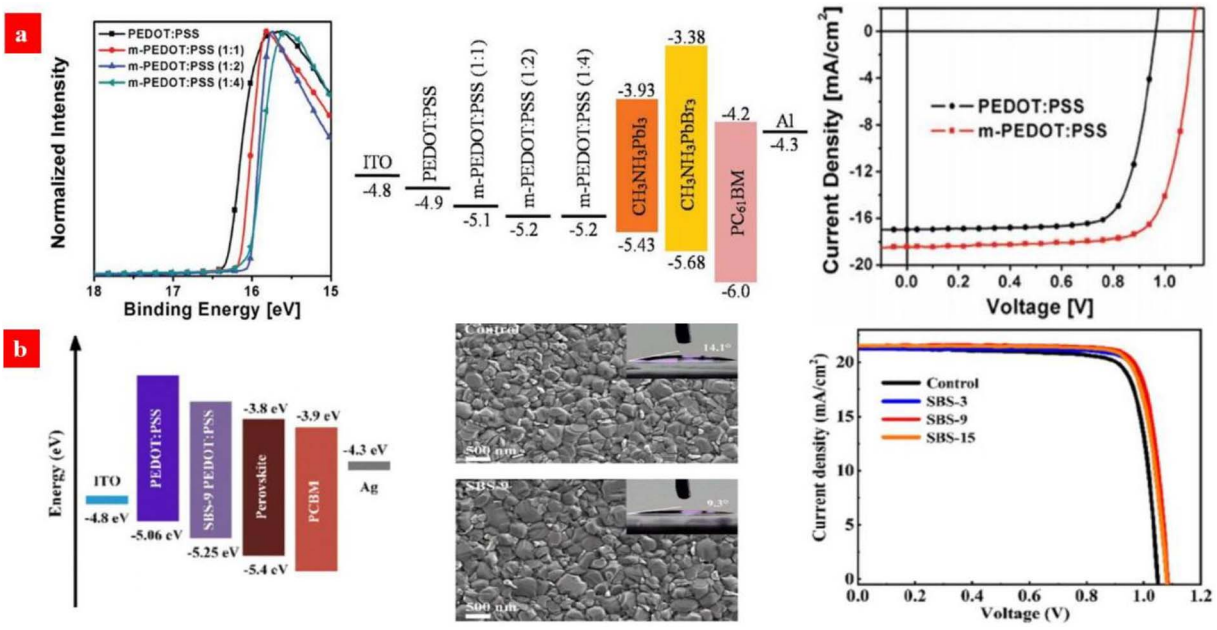

Fig. 4 (a) UPS of PEDOT:PSS and m-PEDOT:PSS films; energy level diagram of the PSCs; and *J*–*V* curves of the PSCs with PEDOT:PSS or m-PEDOT:PSS (1 : 2) as the HTL. Reproduced with permission.[130] Copyright 2017, Wiley-VCH. (b) Energy level diagram of devices; SEM of perovskite active layers deposited on PEDOT:PSS with $C_6H_5SO_3Na$ (9 mg mL^{-1}); and *J*–*V* curves of the devices with the PEDOT:PSS HTLs with $C_6H_5SO_3Na$ (0, 3, 9 and 15 mg mL^{-1}). Reproduced with permission.[131] Copyright 2021, Wiley-VCH.

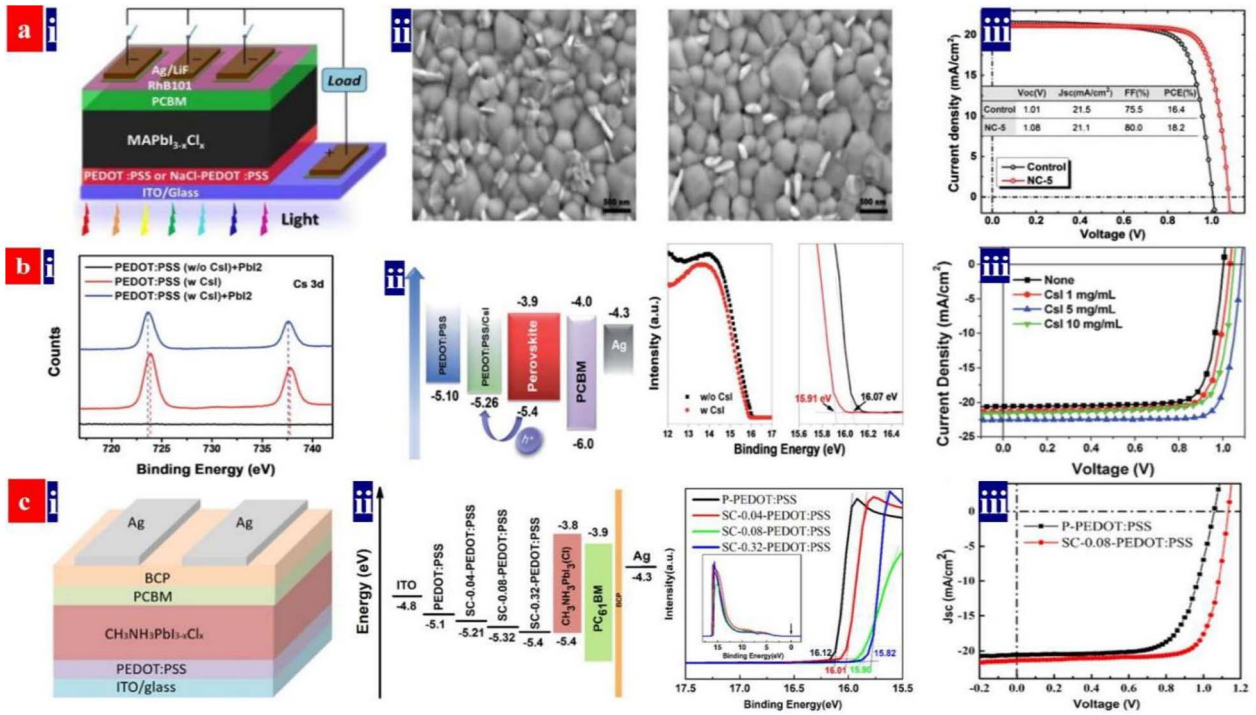

Fig. 5 (a) (i) PSC architecture; (ii) SEM images of perovskite films deposited on pristine PEDOT:PSS and NaCl-PEDOT:PSS; and (iii) J–V curves of the PSCs with pristine or NaCl-doped PEDOT:PSS. Reproduced with permission.[132] Copyright 2017, American Chemical Society. (b) (i) Cs 3d XPS binding energy; (ii) energy level diagram of the PSCs and UPS binding energy of PEDOT:PSS films with and without CsI; and (iii) J–V curves of inverted PSCs processed with PEDOT:PSS containing CsI in different concentrations. Reproduced with permission.[133] Copyright 2019, Royal Society of Chemistry. (c) (i) PSC architecture; (ii) energy level diagram of the PSCs and UPS binding energy of PEDOT:PSS films; and (iii) J–V curves of the inverted PSCs. Reproduced with permission.[134] Copyright 2019, American Chemical Society.

transport. The CsI-treated PEDOT:PSS HTLs enabled a better PSC with a non-radiative voltage loss of 0.287 V, which was superior to the control device with a non-radiative voltage loss of 0.375 V. The best inverted PSCs exhibited a small voltage loss, a high PCE of up to 20.22%, a V_{OC} of 1.084 V and almost no hysteresis; whereas the control ones with the pristine PEDOT:PSS HTLs just delivered a PCE of 16.57% (Fig. 5b). In the future, the effective treatments using CsF, NaF and NaI and combined treatments using the salts and bases can be developed to make the PEDOT:PSS HTLs. Through optimizing the doping concentrations, doping temperatures and processing times, both high-φ PEDOT:PSS HTLs and high-quality perovskite layers have a high probability of achievement for exciton dissociation and charge-carrier transport, thereby leading to an improved PCE of the inverted PSCs.

Recently, Song's group added sodium citrate into the PEDOT:PSS aqueous solutions for PEDOT:PSS HTL preparation.[134] The sodium citrate treatment increased the work function of the HTLs and it made the valence band of perovskite absorbers compatible with the HTLs; besides, upon the sodium citrate treatments, the grain sizes of the perovskite crystals became larger when deposited on the PEDOT:PSS HTLs; meanwhile the perovskite layers were more uniform. On the basis of the sodium citrate-treated PEDOT:PSS HTLs, the PCE of the $CH_3NH_3PbI_3(Cl)$-based PSCs largely increased from 15.05% to 18.39%. The PCE enhancement originated from a simultaneous increase in V_{OC}, short-circuit current density (J_{SC}) and FF (Fig. 5c).

3.3. F4-TCNQ treatment

A surface-modification strategy has emerged to raise the work function and electrical conductivity of the PEDOT:PSS HTLs. For example, Liu *et al.*[135] investigated the effects of a p-type dopant 2,3,5,6-tetrafluoro-7,7,8,8-tetracyanoquinodimethane (F4-TCNQ) on the optoelectrical properties of PEDOT:PSS HTLs and the photovoltaic parameters of inverted PSCs. After adding 0.30 wt% F4-TCNQ into the PEDOT:PSS aqueous solutions, the PEDOT:PSS HTL showed a lower highest occupied molecular orbital (HOMO) level for a high work function of 5.24 eV, and the film exhibited an enhanced conductivity of 0.136 S cm^{-1}. Notably, the favorable energy level alignment and the enhanced conductivity of the F4-TCNQ-doped films allow an efficient carrier transport from the perovskite layer to the HTL. As a result, the inverted PSCs with the 0.30 wt% F4-TCNQ-doped PEDOT:PSS HTL yielded a PCE of 17.22%, which was much higher than that (13.30%) of the control PSCs (Fig. 6).

Owing to the strong electron withdrawing capability of the fluorine atoms of F4-TCNQ, it is captured from the PEDOT materials to increase the number of molecular holes of the polymer matrices. We advise that other p-type molecules involving fluorine atoms, such as 2,2′-(perfluoronaphthalene-2,6-diylidene) dimalononitrile (F6-TCNNQ) and 2,5-tetrafluoro-7,7,8,8-tetracyanoquinodimethane (F2-TCNQ), can be used to modify the PEDOT:PSS films for an efficient charge transfer and a high device efficiency in the future. Besides, it is suggested that

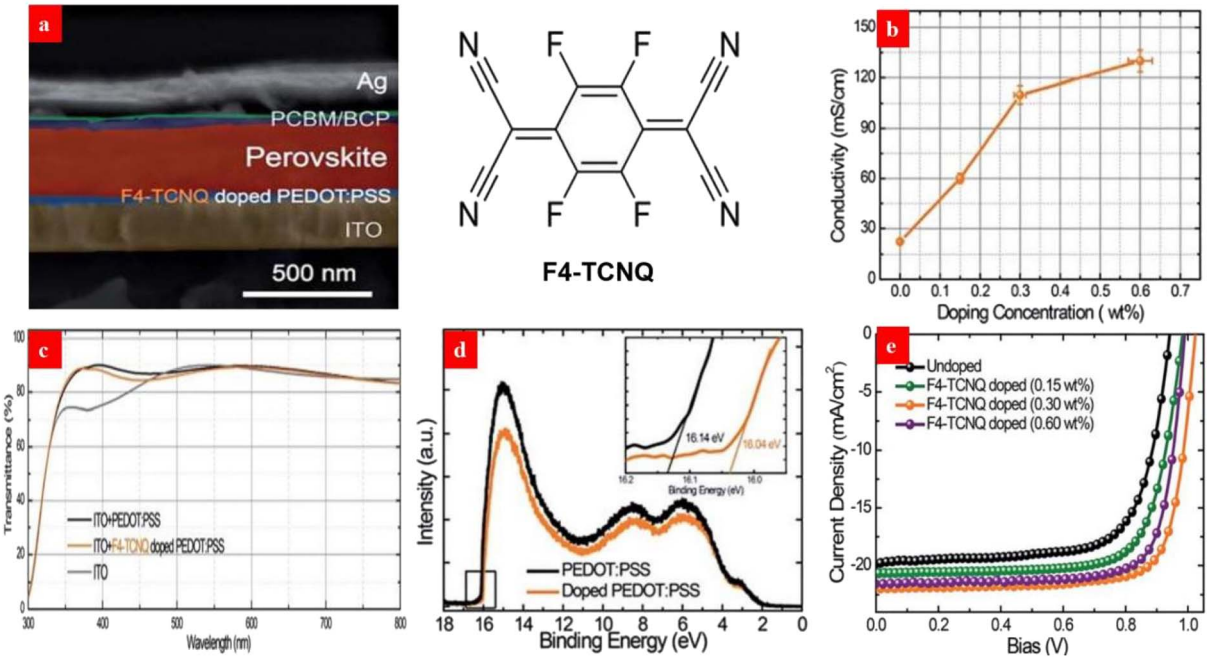

Fig. 6 (a) Cross-sectional SEM of each layer with the chemical structures of F4-TCNQ. (b) Dependence of the film conductivity on the doping concentration. (c) Film transparencies. (d) UPS of the PEDOT:PSS films. (e) *J*–*V* curves of the PSCs with the PEDOT:PSS HTLs. Reproduced with permission.[135] Copyright 2017, Royal Society of Chemistry.

solution-processed metal oxide HTLs such as NiO_x and MoO_3 have a potential to improve the device efficiency and stability through using the similar doping treatments mentioned above.

3.4. DMF, EMIC and urea treatments

Dimethylformamide (DMF) treatments can improve the electrical conductivity of the PEDOT:PSS HTLs *via* reduction of the Coulomb interactions between PEDOT and PSS. Chen *et al.*[136] employed the DMF-treated PEDOT:PSS HTLs and polymethyl methacrylate (PMMA)-modified PCBM ETLs to establish a charge-carrier balance in the p-i-n PSCs. The electrical conductivity ($\approx 10^{-1}$ S cm^{-1}) of the DMF-treated PEDOT:PSS thin films were higher than that ($\approx 10^{-3}$ S cm^{-1}) of as-cast thin films. The higher conductivity of the PEDOT:PSS films facilitated an interfacial contact between the perovskite layers and

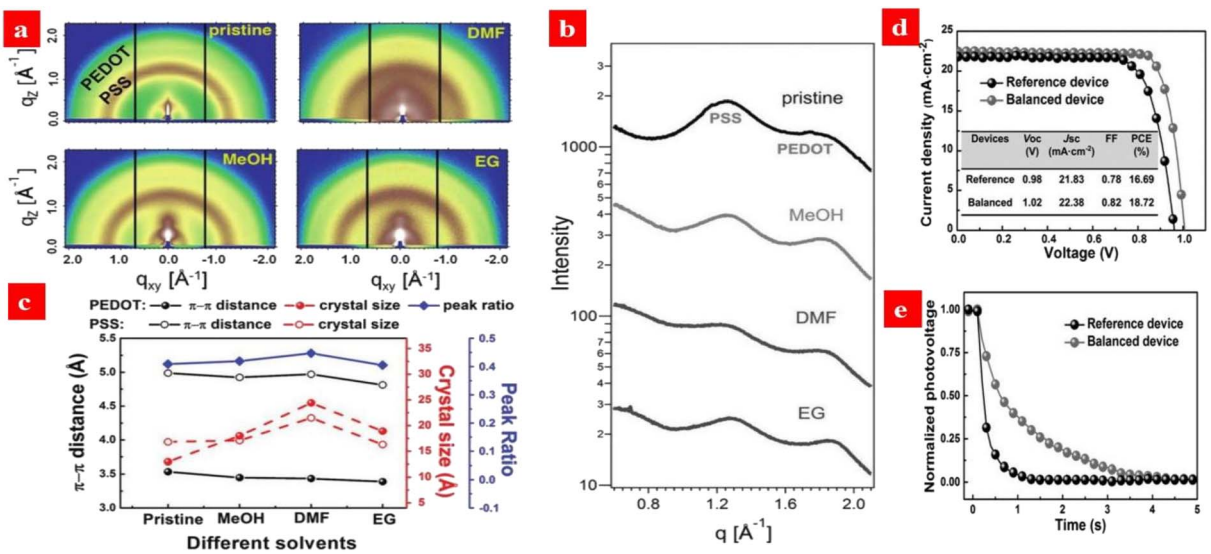

Fig. 7 (a) 2D GIWAXS measurements of PEDOT:PSS films treated by different solvents. (b) Sector integrals of the 2D GIWAXS data. (c) An overview of the crystallite sizes, stacking distances, and the PEDOT ratios in PEDOT:PSS films treated by different solvents. (d) *J*–*V* curves of the PSCs. e Open-circuit photovoltage-decay measurements. Reproduced with permission.[136] Copyright 2016, Wiley-VCH.

PEDOT:PSS HTLs. As shown in Fig. 7, the PEDOT crystal sizes varied from 1.30 nm (as-cast ones) to 2.44 nm (DMF-treated ones), and the large crystal size could be attributed to a diffusion of the organic solvents into PEDOT:PSS matrices and a low π–π stacking distance of PEDOTs.[136,137] The resultant PSCs yielded a high PCE of 18.72%. An inspiring result is that the V_{OC} had a slower photovoltage decay than the reference, suggesting a lower charge-carrier-recombination rate and more balanced charge-carrier transport.[137]

In terms of ionic liquid (IL) doping treatments, Zhou *et al.*[138] developed a novel synergistic strategy that uses 1.5 wt% EMIC (1-ethyl-3-methylimidazolium chloride) ionic liquid to modify the PEDOT:PSS HTLs. It enables a HTL with an improved electrical conductivity of up to 200 S cm^{-1}, a relatively low work function of 5.18 eV and a smooth surface. This doping treatment helps to extent the carrier recombination life time and it reduces the charge trap density of the perovskites. As a result, the champion photovoltaic cells showed 20.06% PCE without hysteresis (Fig. 8).

In order to improve the conductivity as well as work function of the PEDOT:PSS HTLs, Elbohy *et al.*[139] demonstrated a urea treatment that effectively tuned the phase-separated morphology of the PEDOT:PSS HTLs. After the urea treatment, the coulombic interaction between the PEDOT and PSS segments was dramatically decreased and it allowed for a better phase separation between the conductive PEDOT and the insulating PSS regions. As a result, the 5 wt% urea-treated PEDOT:PSS films had a nanofibril-like morphology; and the films showed an electrical conductivity of 12.75 S cm^{-1}. In contrast, the electrical conductivity was only 0.20 S cm^{-1} for the pristine films. The enhanced conductivity was mainly induced by the better phase-separated morphology with the rich nanofibrils. Urea also inhibited the counter-ion exchange interaction between the PEDOT:PSS and perovskites by transforming PSS-H into PSS-NH_4 for a better PSC. The device PCE was increased from ≈14.4% to ≈18.8%.

3.5. Component strategies

It is promising to invent an efficient inverted PSC *via* employing a component HTL that consists of PEDOT:PSS (P VP AI 4083), metal oxides and organic materials (*e.g.*, PTAA).[140,141] For example, Choi *et al.*[140] reported a flexible inverted PSC using PEDOT:PSS (P VP AI 4083) and MoO_3 as a component HTL. The 2.0 nm-thick thin layers of MoO_3 enabled an efficient hole doping into graphene electrodes. The PEDOT:PSS and MoO_3 components had the suitable energy levels for effective hole transport. The resultant PSCs showed a PCE of ≈16.8% without visible hysteresis, which was slightly lower than that (≈17.3%) of the control PSCs fabricated on ITO/glass. Next, Zang's group[142] proposed a facile passivation approach that employed an ultrathin PTAA layer to passivate the interfacial and grain boundary defects (Fig. 9). This PTAA is sandwiched between the

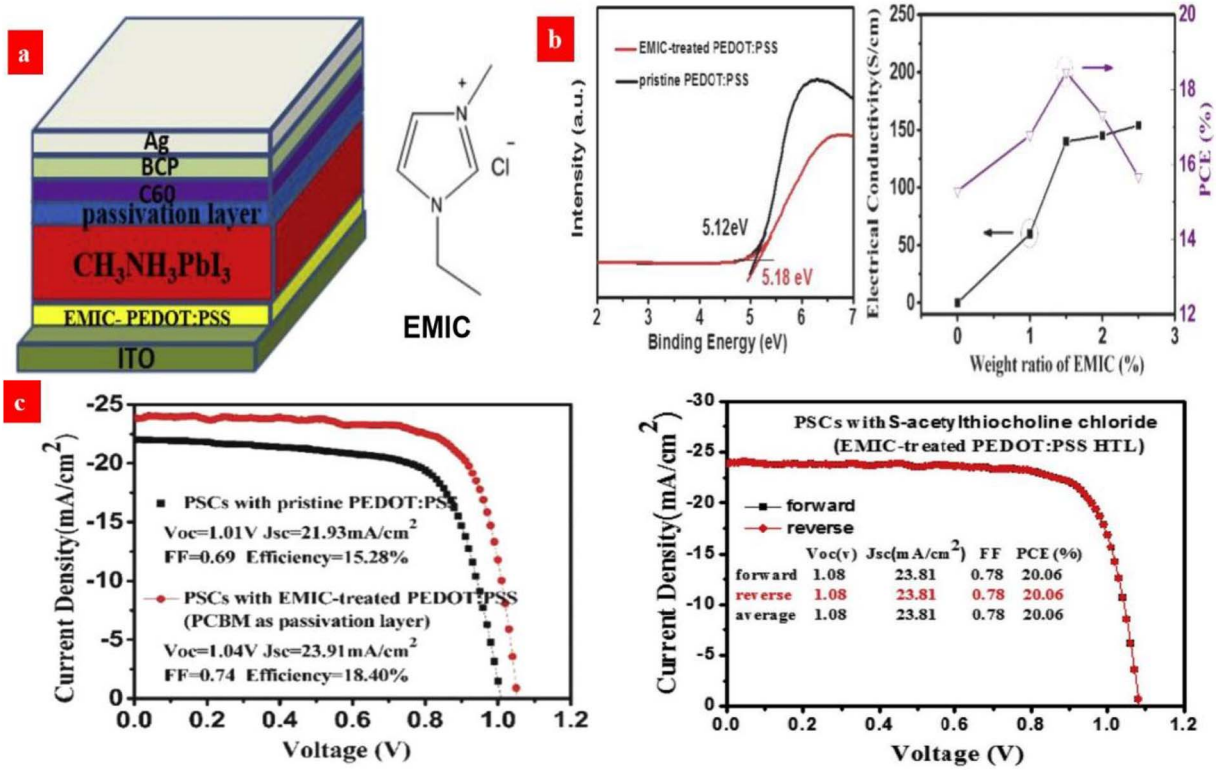

Fig. 8 (a) Configuration of an inverted PSC device and the molecular structure of EMIC. (b) UPS spectra of pristine and EMIC-treated PEDOT:PSS films, and electrical conductivities of PEDOT:PSS HTL. (c) *J*–*V* curves of the PCBM-based PSCs with the pristine and EMIC-treated PEDOT:PSS HTL, and the best PSCs with both EMIC-PEDOT:PSS HTL and S-acetylthiocholine chloride passivation layer. Reproduced with permission.[138] Copyright 2019, Elsevier.

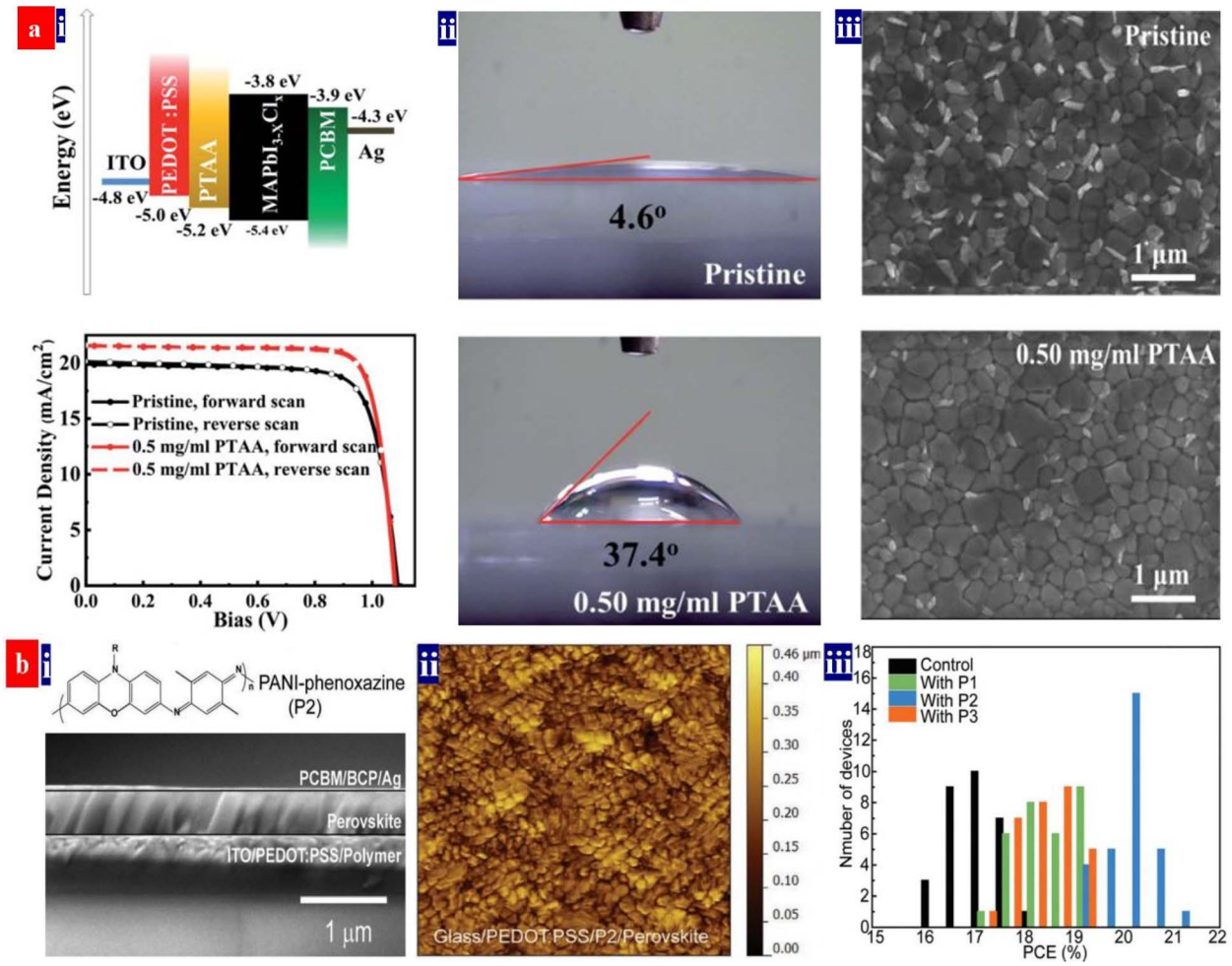

Fig. 9 (a) (i) Energy level diagram, and the typical J–V curves of the inverted PSCs, (ii) contact angles of the PEDOT:PSS HTLs modified by PTAA: 0 mg mL^{-1} (top) and 0.50 mg mL^{-1} (bottom) and (iii) SEM images of the perovskite films. Reproduced with permission.[142] Copyright 2019, Royal Society of Chemistry. (b) (i) the cross-sectional SEM image of the MAPbI3 inverted PSCs with the P2, (ii) AFM images of perovskite films on various PEDOT:PSS substrates, and (iii) the PCE distribution of the inverted PSCs. Reproduced with permission.[4] Copyright 2022, Wiley-VCH.

perovskites and the HTLs to suppress interfacial recombination and accelerate hole transfer. An energy band alignment was realized by introducing this ultrathin PTAA layer. As a result, the inverted PSCs yielded a considerably high PCE of 19.04% with FF of 82.59% and J_{SC} of 21.38 mA cm^{-2}. In the future, the methodologies of HTLs fabricated from composites of PEDOT:PSS deserve further rigorous pursuit towards greater improvement of for an energy band alignment and an intimate contact at interfaces. The energy band alignment among transparent electrodes, HTLs and perovskites can suppress the interfacial recombination and accelerate the hole transfer, resulting in a high PCE of the inverted PSCs.

Otherwise, Ma *et al.*[143] introduced a triphenylamine-based small molecule, *N*,*N*′-bis-(1-naphthalenyl)-*N*,*N*′-bis-phenyl-(1,1-biphenyl)-4,4′-diamine (NPB), into the inverted PSCs as the multifunctional buffer layer (Fig. 10). The NPB buffer layer inserted not only restrains a formation of pin-holes and defects of the perovskites, but also it reduces the energy level mismatch between the perovskites and PEDOT:PSS HTLs. As a result, the devices showed a reduced trap density and a prolonged carrier lifetime, which led to an increase of the PCE from 15.4% to 18.4% without hysteresis. It should be mentioned that the inverted PSCs with the NPB/PEDOT:PSS HTLs possessed a relatively long-term stability under ambient air and under UV-light irradiation, which was attributed to the superior moisture and UV-light resistance of the NPB layers that shielded the PEDOT:PSS bottom layers.

These aforementioned modification treatments and component strategies significantly improve the PCEs of the inverted PSCs. Table 3 summarizes the photovoltaic characteristics of the inverted PSCs based on the PEDOT:PSS HTLs reported recently. In the future, a higher charge-carrier mobility and a better balance between hole mobility (μ_h) and electron mobility (μ_e) are highly derisible for the development of highly efficient and stable inverted PSCs; and we envision that the high-performance photovoltaic cells will be realized by the pathways, *e.g.*, HTL and ETL co-modifications, a perovskite passivation, an insertion of insulating ultrathin layers (*e.g.*, PMMA and Al_2O_3), *etc.* Finally, an ideal PEDOT:PSS HTL needs to stabilize its electronic structure, electrical conductivity, work

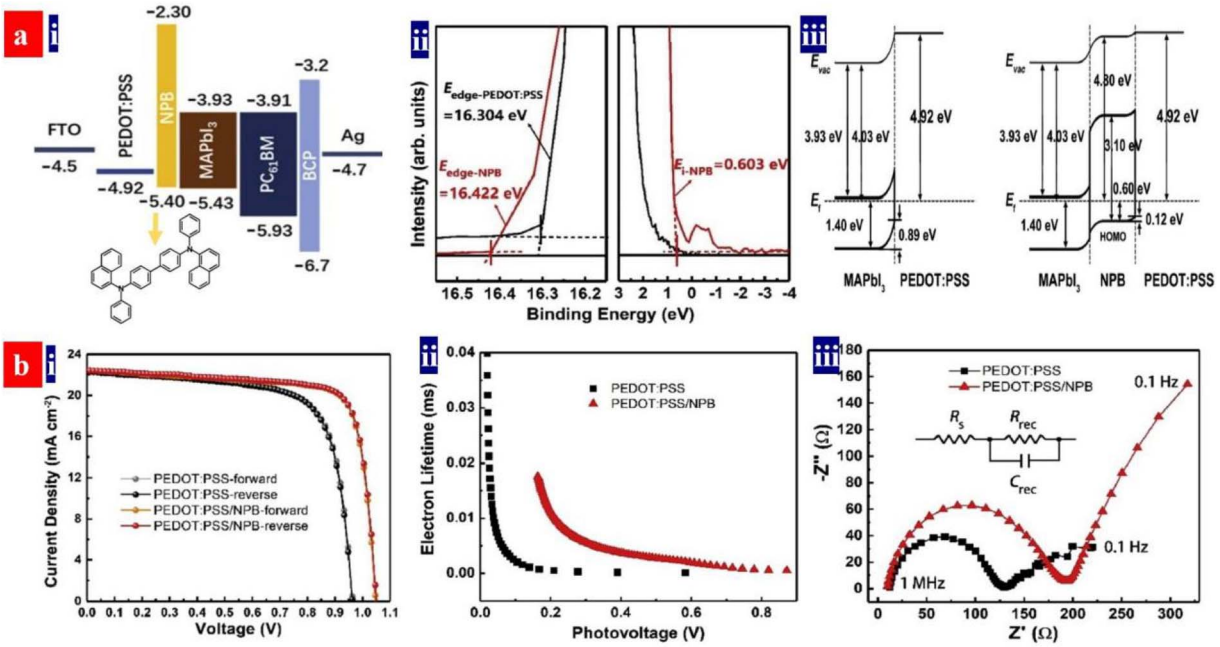

Fig. 10 (a) (i) Energy level diagram and molecular structure of NPB; (ii) UPS of the PEDOT:PSS HTLs; and (iii) energy level alignment diagrams at PEDOT:PSS/$MAPbI_3$ and PEDOT:PSS/NPB/$MAPbI_3$ interfaces. (b) (i) *J*–*V* curves of the inverted PSCs; (ii) extracted lifetime of the injected carriers *versus* photovoltage; and (iii) electrical impedance spectroscopy spectra. Reproduced with permission.[143] Copyright 2022, Elsevier.

function and morphology, which are indeed very critical to the operation stability of the photovoltaic cells as well as an intimate contact with the perovskite layers on tops.

4. Perovskite photodetectors with PEDOT:PSS

Photodetectors probe various optical signals from background radiation and then convert them to various electrical signals. The devices have a promising application in high-speed optical communication and high-resolution imaging.[144] Halide perovskite materials have received much research interest in photodetector fields, owing to their excellent optoelectronic properties of appropriate direct bandgaps, high light absorption coefficients and long carrier transport lengths.[144–146] Halide perovskite photodetectors have three types: photoconductors, photodiodes and phototransistors.[146–150] This section focuses on the perovskite-based photodetectors with the PEDOT:PSS thin films. It illustrates the key roles of the PEDOT:PSS on the device performances. Finally, suggestions are provided for potentially guiding the development of future photodetectors based on PEDOT:PSS.

4.1. Phototransistors with Perovskite/PEDOT:PSS heterojunctions

Organolead halide perovskites suffer from low gains in comparison with phototransistors based on other functional materials. Moreover, a detectable wavelength region is limited by a bandgap issue of the perovskites. Yan's group demonstrated a broadband phototransistor with $MAPbI_{3-x}Cl_x$/PEDOT:PSS (Clevios™ PH500) heterojunctions.[151] Under light illumination, excitons were generated in the $MAPbI_{3-x}Cl_x$ matrices. Then, the holes diffused into the PEDOT:PSS layer because of an decreased energy; while the electrons accumulated in the $MAPbI_{3-x}Cl_x$ films since the conduction band of the $MAPbI_{3-x}Cl_x$ materials was lower than the lowest unoccupied molecular orbital (LUMO) level of the PEDOT:PSS materials. Most of the channel currents originate from the hole transport in the PEDOT:PSS thin layers. The currents across the perovskite layers are extremely small. It is supposed that the DMF from the perovskite solutions indeed improves the electrical conductivity of the PEDOT:PSS films, leading to a high hole mobility and an effective hole transport in PEDOT:PSS matrices. The PD devices showed a high responsivity (R) of 10^9 A W^{-1} and a specific detectivity (D^*) of 10^{14} Jones in spectral response ranges of 350–1100 nm at 0.5 V operating bias. In such an innovative phototransistor, the photo-generated electrons are not necessarily mobile in the perovskite films. Thus, a high R in the near infrared (NIR) region could be achieved.

The spectral response range of typical $MAPbI_3$-based PDs is generally limited owing to the relatively wide optical bandgap. The perovskite materials with smaller optical bandgaps can be realized by the blends of halogen ions, the blends of Sn and Pb, Cs-doped $FAPbI_3$, *etc.*[145–157] It should be mentioned that the leads in the perovskite materials can potentially cause severe human health and environmental problems, hampering a practical application of the PDs. Yan's group demonstrated a photodetector with a tin-based perovskite/PEDOT:PSS (Clevios™ PH500) vertical heterojunction (Fig. 11).[157] The $FASnI_3$/PEDOT:PSS device showed a broadband photo-response from NIR to UV, a high responsivity of 2.6×10^6 A W^{-1}, gain of

Table 3 Photovoltaic performances of inverted PSCs with PEDOT:PSS HTLs

Device structure	Method and recipe	φ (eV)	σ (S cm^{-1})	V_{OC} (V)	J_{SC} (mA cm^{-2})	FF	PCE	Ref.	Year
FTO/PEDOT:PSS/P2/$MAPbI_3$/$PC_{61}BM$/BCP/Ag	Deposition of P2 on PEDOT:PSS	5.37	—	1.13	23.56	0.791	21.06%	4	2022
ITO/PC-PEDOT/$MAPbI_3$/$PC_{61}BM$/BCP/Ag	0.035 M potassium citrate treatment	4.55	—	1.099	21.93	0.819	19.66%	129	2021
ITO/$C_6H_5SO_3Na$-PEDOT:PSS/$MA_{0.8}FA_{0.2}PbI_{3-x}Cl_x$/$PC_{61}BM$/Ag	9 mg mL^{-1} $C_6H_5SO_3Na$ treatment	5.25	—	1.08	21.52	0.801	19.41%	131	2021
ITO/PEDOT:PSS-WO*x*/$MAPbI_3$/$PC_{61}BM$/ZnO/Al	Deposition of WO_x on PEDOT:PSS	—	—	1.08	22.78	0.804	19.64%	128	2020
FTO/PEDOT:PSS/NPB/$MAPbI_3$/$PC_{61}BM$/BCP/Ag	15 nm-thick BCP modification	5.40	—	1.05	22.46	0.780	18.40%	143	2020
ITO/SC-PEDOT/$CH_3NH_3PbI_3$(Cl)/$PC_{61}BM$/BCP/Ag	0.08 M sodium citrate treatment	5.32	—	1.134	21.62	0.750	18.39%	134	2019
ITO/CsI-PEDOT:PSS/$MAPbI_3$/$PC_{61}BM$/Ag	5 mg mL^{-1} CsI treatment	5.26	—	1.08	22.59	0.83	20.22%	133	2019
ITO/urea-PEDOT:PSS/$MAPbI_3$/$PC_{61}BM$/Rhodamine/Ag	0.5 wt% urea treatment	—	12.75	1.03	22.57	0.809	18.80%	139	2019
ITO/PEDOT:PSS/$MAPbI_3$/$PC_{61}BM$/C_{60}/BCP/Ag	1.5 wt% EMIC treatment	5.18	200	1.04	23.91	0.74	18.40%	138	2019
ITO/PEDOT:PSS/$MAPbI_3$/S-acetylthiocholine chloride/C_{60}/BCP/Ag	1.5 wt% EMIC treatment	5.18	200	1.08	23.81	0.78	20.06%	138	2019
ITO/F4-TCNQ-PEDOT:PSS/$CH_3NH_3PbI_{3-x}Cl_x$/$PC_{61}BM$//BCP/Ag	0.3 wt% F4-TCNQ modification	5.18	0.11	1.02	21.73	0.77	17.22%	135	2017
ITO/DMF-PEDOT:PSS/$MAPbI_3$/$PC_{61}BM$/PMMA/BCP/Ag	DMF rinsing	—	—	0.98	22.70	0.81	18.02%	136	2016
ITO/DMF-PEDOT:PSS/$MAPbI_3$/$PC_{61}BM$/BCP/Ag	DMF rinsing; 1.0 wt% PMMA modification	5.12	10^{-1}	1.02	22.38	0.82	18.72%	136	2016

4.7×10^6 and specific detectivity of 3.2×10^{12} Jones. The high responsivity was attributed to the long carrier lifetime and strong light absorption of the perovskites and the strong photo-gating effect. The photo-gating effect stemmed from the perovskite/PEDOT:PSS vertical heterojunction. In the future, through adjusting the LUMO or Fermi levels of the PEDOT:PSS thin films and raising the hole mobility, the perovskite PD performances could be potentially further enhanced due to a raised capability of charge separation and hole transport.

4.2. X-ray detectors with PEDOT:PSS HTLs

X-ray detectors have applications in the structural determinations of crystals, noninvasive imaging, security inspection, medical radiography, and nuclear power stations.[158] Perovskites can detect the ultraviolet-visible-near infrared (UV-vis-NIR) photons and the high-energy X-rays and γ-rays. The heave atoms of Pb, I and Br dominate the high-energy photon absorption; then, the high-energy photons with a strong penetrating capability enable a carrier generation across the crystals. According to $\alpha \propto Z^4/E^3$, the atomic number (Z) determines the attenuation coefficient (α), where E is the photon energy. To ensure an efficient charge collection of the detector, it requires a large charge carrier mobility (μ) − charge carrier lifetime (τ) product, a high resistivity and a low charge trap density.[159]

Heiss's group previously proposed a concept of applying $MAPbI_3$ semiconductors for the X-rays detection.[160] The $MAPbI_3$ photoconductors with the PEDOT:PSS HTLs showed an almost ideal photo-response in the NIR to vis ranges, a fast response time and a high absorption cross-section for X-rays owing to the heavy Pb and I atoms. Notably, a high-quality $MAPbBr_3$ layer was also deposited on hydrophobic PTAA instead of the PEDOT:PSS HTLs.[161] Recently, the PEDOT:PSS HTLs were used to fabricate broadband photodetectors with a component active layer that consists of $CH_3NH_3PbI_3$ and $CuInSe_2$ quantum dots (CISe QDs) (Fig. 12a).[162] The component active layer absorbs radiation, generates the electron–hole pairs, and then transports the holes from the perovskites and CISe QDs to the HTLs due to gradient energy alignment.[162] The HOMO level of the PEDOT:PSS is slightly shallower than the valence band position of the CISe QDs, which is energetically favorable for holes transfer and extraction. The photodetector delivered a broadband response from the UV to the NIR. Notably, the perovskites showed an optical response from the UV to vis regions, while the CISe QDs provided a light response in the NIR regions. The best photodetector exhibited a responsivity of 193 mA W^{-1} at 580 nm and >20 mA W^{-1} in the NIR region of 800–1000 nm. The device had a D^* of $>7.0 \times 10^{12}$ Jones in the vis and 7.7×10^{11} Jones in the NIR with a transient response time of 277 ns. In a previous literature,[163] the $CuInSe_2$ QDs and PEDOT:PSS emerged as a hybrid HTL of the perovskite photodetectors (Fig. 12b). The $CuInSe_2$ QDs increased the HTL wettability for a better growth of perovskite crystals. Additionally, the QDs blocked the electron transfer from perovskites to PEDOT:PSS.[163] The resultant devices with the $CuInSe_2$ QDs and PEDOT:PSS hybrid HTLs showed a photoresponsivity of 240 mA W^{-1} at 580 nm and a maximum detectivity of 1.02×10^{13} Jones at 580 nm.

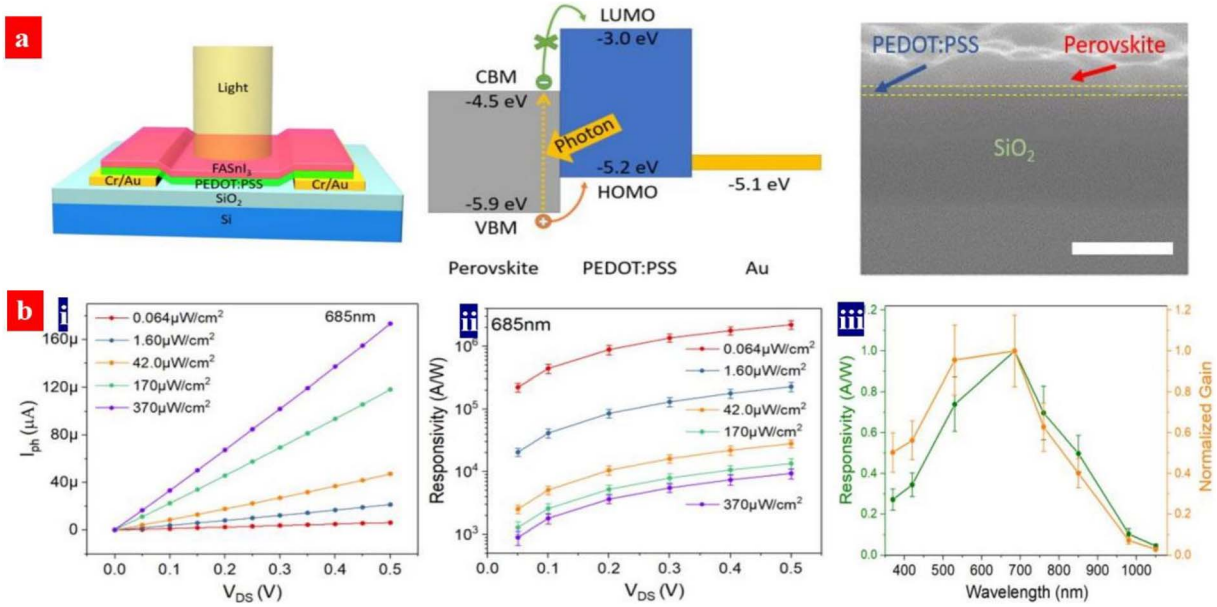

Fig. 11 (a) Architecture structure of the PDs, energy band diagram, and cross-sectional SEM image of (a) $FASnI_3$/PEDOT:PSS bilayer coated on SiO_2/Si. Scale bar: 300 nm. (b) (i) Photo-current *vs.* drain voltage; (ii) average responsivity *vs.* drain voltage under various intensity of light. Wavelength: 685 nm; and (iii) normalized spectral responsivity and gain of the PD. Reproduced with permission.[157] Copyright 2020, American Chemical Society.

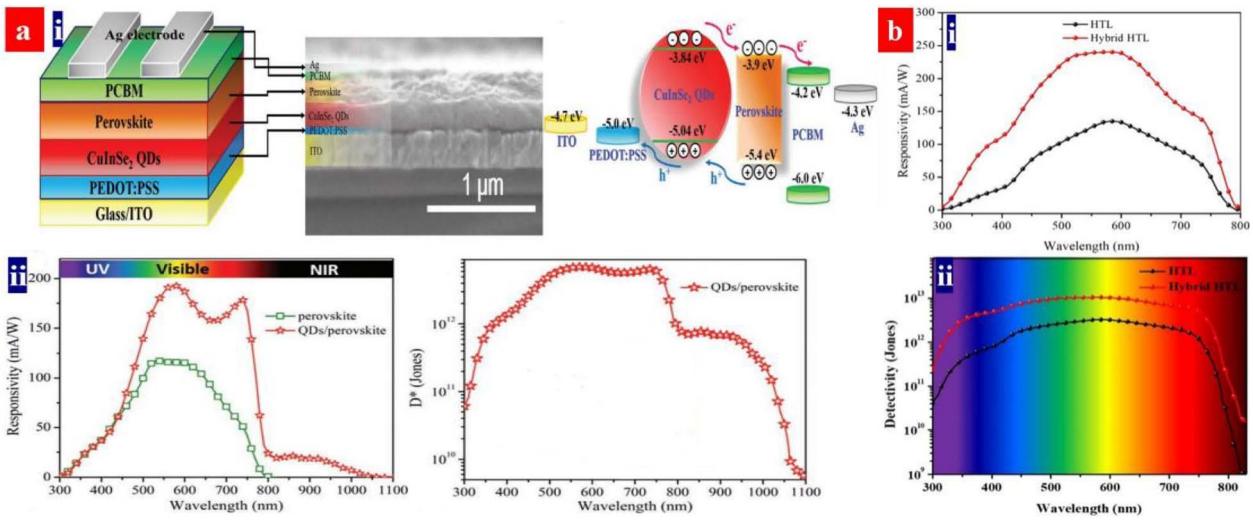

Fig. 12 (a) (i) Architecture structure, cross-sectional SEM image and energy band diagram of the PDs. (ii) Responsivity and specific detectivity spectra at 0 V bias voltage. Reproduced with permission.[162] Copyright 2020, Wiley-VCH. (b) Responsivity (i) and specific detectivity (ii) of the devices with the hybrid HTL and PEDOT:PSS HTL, respectively, at 0 V bias voltage. Reproduced with permission.[163] Copyright 2018, American Chemical Society.

However, optoelectronics with organic functional layers generally suffered from a stability concern. In 2022, Fan *et al.* proposed a silver bis(trifluoromethanesulfonyl)imide (AgTFSI) treatment that was used to chemically dope the PEDOT:PSS HILs.[91] AgTFSI acts as an effective p-dopant for a high charge concentration. It improved the work function and surface potential of the PEDOT:PSS HILs for an interface energy band alignment. The colloidal red QD-LEDs not only yielded a high external quantum efficiency but also exhibited an excellent operation stability in ambient air with a T_{95} (time for the device brightness to decrease to 95% of its initial brightness) of 4160 hours at an initial brightness of 1000 cd m^{-2}. It is envisioned that similar ionic liquid salt-doping strategies have a great potential to promote the stability of the photodetectors based on the PEDOT:PSS HTLs. In addition, PEDOT:PSS HTLs can be used to fabricate fiber-shaped photodetectors constructed by vertical organic-inorganic heterostructures of zinc oxide/poly(3-hexylthiophene) (P3HT).[38] To achieve rapid hole transport, the

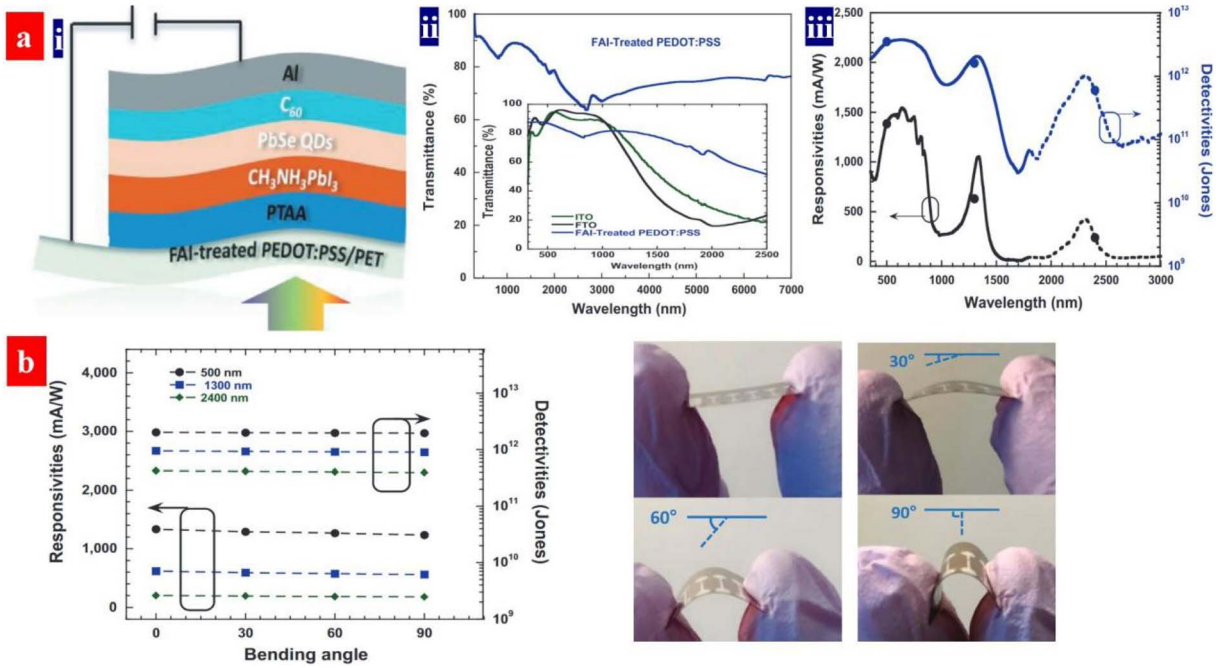

Fig. 13 (a) (i) Device architecture, (ii) transmittance spectra of the PEDOT:PPS electrodes, and (iii) responsivities and detectivities of flexible devices *versus* wavelength. (b) Responsivities and detectivities *versus* bending degree at a bias of −1 V and the device photographs under a bending angle of 0°, 30°, 60°, and 90°, respectively. Reproduced with permission.[165] Copyright 2020, Wiley-VCH.

surface of vertical ZnO/P3HT heterostructure was covered with the thin PEDOT:PSS layer, and the device showed a high responsivity of 156 μA W^{-1}, high specific detectivity of 0.74 × 10^9 Jones, and a short response/recovery time of <40 ms under zero bias for 365 nm light illumination (32.5 mW cm^{-2}). Other fiber-shaped perovskite PDs can be realized in light of the work based on vertical organic-inorganic heterostructures.[38]

4.3. Flexible photodetectors with PEDOT:PSS transparent electrodes

ITO films are the most commonly used transparent electrodes for various electronics owning to their high optical transparencies (about 90% transparency in the visible region) and low sheet resistances (10–30 Ω sq^{-1}). However, the ITO transparent electrodes are brittle and expensive, making them unsuitable for flexible electronics. Moreover, the ITO films have a weak transmittance in IR regions,[164] which are unsuitable to the PDs with broadband detection as a flexible transparent electrode. In addition, the solution-processed PEDOT:PSS electrodes have the advantages of high optoelectrical characteristics and good flexibility over those of the ITO coated onto thermoplastics substrates.

Recently, Gong's group demonstrated a room-temperature solution-processed flexible photodetector with a spectral response from 300 to 2600 nm,[165] as shown in Fig. 13. The flexible photodetector possessed a vertical device structure incorporating a perovskite/PbSe QD photoactive layer and a PEDOT:PSS transparent electrode. The PEDOT:PSS electrode was treated by 100 μL of formamidinium iodide (FAI) solutions (dimethylformamide as solvents). After the FAI treatment, the conductivity of the electrode was raised to 1275 S cm^{-1}. By means of a trap-assisted photomultiplication effect, the perovskite/PbSe photoactive layer showed a spectral response to the IR region and an improved photocurrent density in the Vis and IR regions. Under an external bias of −1.0 V, the flexible photodetectors exhibited over 230 mA W^{-1} responsivity, over 1011 cm $Hz^{1/2}$ W^{-1} photodetectivity from 300 to 2600 nm and 70 dB linear dynamic ranges.

The electrical conductivity of the FAI-treated PEDOT:PSS transparent electrodes is over 1000 S cm^{-1}.[165] However, the electrical conductivity and optical transmittance of the PEDOT:PSS films are not high enough for effective charge collections. We advise that the strong acid-treated PEDOT:PSS electrodes serve as a flexible transparent electrode of the PDs, because of the dramatical raise of the electrical conductivity over 4000 S cm^{-1} and a large removal of sulfonates for both higher transparency and better stability. Although most of strong acid treatments are certainly detrimental to the underlying thermoplastic substrates and the treatments caused many acid residuals on PEDOT:PSS surfaces, the gentle acid treatments at low temperature developed recently by Fan *et al.*[94,99] have solved the corrosion issues. In the as-proposed gentle treatments, extremely low-concentration (0.1–0.8 M) strong acid/superacid aqueous solutions are used. Especially, the doping temperature is as low as 20–50 °C. In addition, alcohol solvents are employed to soak and more fully wash off the residual acids.

5. Thermoelectric devices based on PEDOT:PSS and its components

The thermoelectric properties of a given material are usually evaluated by the dimensionless figure of merit (ZT), $ZT = S^2\sigma T/$

k, where S is the Seebeck coefficient, σ is the conductivity, T is the absolute temperature and k is the thermal conductivity. $S\sigma^2$ is defined as the power factor (PF). Because of the high conductivity, the PEDOT:PSS materials can exhibit high thermoelectric properties. In comparison with the conventional thermoelectric materials that are inorganic semimetals or semiconductors, thermoelectric polymers like PEDOT:PSS have the unique merits including low intrinsic thermal conductivity, low cost, no or low toxicity, and high mechanical flexibility.[166,167] Both high electrical conductivity and Seebeck coefficient are required for employment in thermoelectric devices.

The electrical conductivity of PEDOT:PSS can be greatly enhanced through secondary doping particularly the post acid treatment. Fan *et al.* carried out the secondary doping of PEDOT:PSS with a DMF solution of an inorganic salt like $ZnCl_2$, $CuCl_2$, $InCl_3$, LiCl, $NiCl_2$ or NaI.[168] This can enhance the conductivity from 0.2 to >1400 S cm^{-1} and the Seebeck coefficient from 14–16 to 26.1 μV K^{-1}. The power factor is thus enhanced to 98.2 μW m^{-1} K^{-2}. The thermoelectric properties of PEDOT:PSS can be further enhanced when a solution with DMF and thionyl chloride ($SOCl_2$), respectively. For example, Zhang *et al.* used methylammonium iodide (MAI) solutions in co-solvents of 80 vol% DMF-20 vol% water for the secondary doping of PEDOT:PSS.[169] It can enhance the conductivity to 1830 S cm^{-1} and Seebeck coefficient to 28 μV K^{-1}. The corresponding PF was 144 μW m^{-1} K^{-2}. In 2021, Fan and co-workers demonstrated a flexible TE based on >99 wt% $SOCl_2$-treated PEDOT:PSS electrodes.[96] The simple $SOCl_2$ treatment enabled a homogeneous and smooth PEDOT:PSS film with a conductivity of 2230 S cm^{-1}, a Seebeck coefficient of 22.8 μV K^{-1}, and a high work function of 4.89 eV. The flexible TEs yielded a PF of 115.9 μW m^{-1} K^{-2}, which was higher than that (91.3–104.0 μW m^{-1} K^{-2}) of the four kinds of the rigid PEDOT:PSS TEs with acid and NaOH multistep treatments. Although secondary doping can significantly enhance the conductivity, it hardly affects the Seebeck coefficient. For example, although a post treatment with H_2SO_4 led to a conductivity of higher than 3100 S cm^{-1}, the Seebeck coefficient was only 16.5 μV K^{-1} and the power factor was 84 μW m^{-1} K^{-2}.[170]

Both conductivity and Seebeck coefficient indeed depend on the charge carrier density or doping level of the conducting polymers. Dedoping is feasible way to visibly increase the Seebeck coefficient although the conductivity is decreased.[171] PEDOT:PSS can be dedoped with a reducing agent or base. Fan *et al.* reported the sequential treatments with H_2SO_4 and NaOH to increase the thermoelectric properties of PEDOT:PSS.[170] As shown in Fig. 14, the NaOH treatment partially dedoped the PEDOT:PSS films. Hence, it increases the Seebeck coefficient and lower the electrical conductivity. At the optimal power factor of 334 μW m^{-1} K^{-2}, the conductivity was 2170 S cm^{-1}, and Seebeck coefficient was 39.2 μV K^{-1}.

Apart from chemical or electrochemical dedoping, dedoping of PEDOT:PSS can occur by light-induced electron transfer between a n-type filler and PEDOT:PSS. Yue *et al.* found that the exposure of PEDOT:PSS/TiO_2 composites to UV light did increase the Seebeck coefficient from 23.5 to 94.3 μV K^{-1}.[172] TiO_2 can absorb UV light, and the excited electrons can transfer

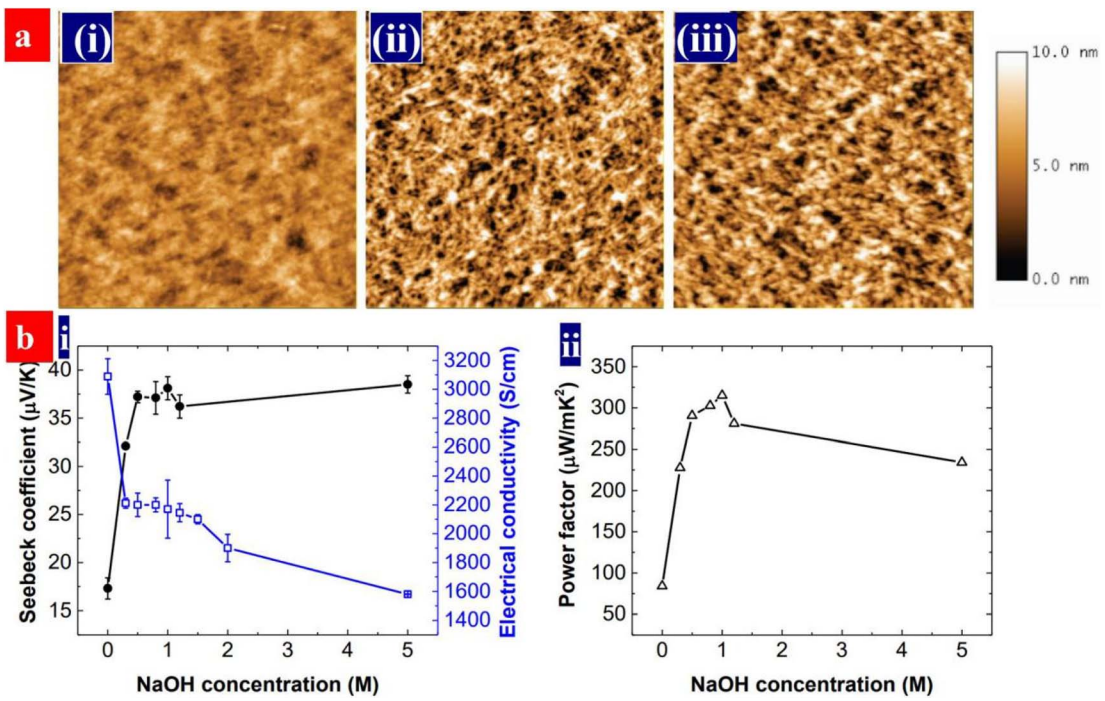

Fig. 14 (a) AFM of the films, that are, (i) as-cast, (ii) H_2SO_4-treated, and (iii) H_2SO_4 and 0.5 M NaOH-treated PEDOT:PSS films. Scale bar: 2 μm × 2 μm. (b) (i) Seebeck coefficients and conductivities, and (ii) power factors of the PEDOT:PSS films with the NaOH concentration. The PEDOT:PSS films were treated with 1 M H_2SO_4 for three times and sequentially with NaOH solution. The NaOH concentration at 0 refers to the films without the NaOH treatment. Reproduced with permission.[170] Copyright 2017, Wiley-VCH.

from TiO_2 to PEDOT:PSS and thus dedope PEDOT:PSS. This is different from the light effect on the Seebeck coefficient of thermoelectric materials. Light exposure hardly affects the Seebeck coefficient of materials with high thermoelectric properties, while it decreases instead of increasing the Seebeck coefficient of some materials with low thermoelectric properties. They called the light-induced increase in the Seebeck coefficient as photo-enhanced Seebeck effect. This was also observed on the composites of PEDOT:PSS with two-dimensional potassium poly-(heptazine imide) (KPHI).[173]

Although dedoping can increase the Seebeck efficient, it is at the sacrifice of the conductivity. A remedy to improve the Seebeck coefficient but not remarkably lower the conductivity is energy filtering. Energy filtering has been reported in polymer and inorganic composites.[167] Its principle is related to the internal electric field at the interface between the electronic matrix and fillers with different Fermi levels. Because the internal electric field can block the accumulation of charge carriers with low energy at the hot or cold end, it can increase the mean energy (E_J) of the accumulated charge carriers. Thus,

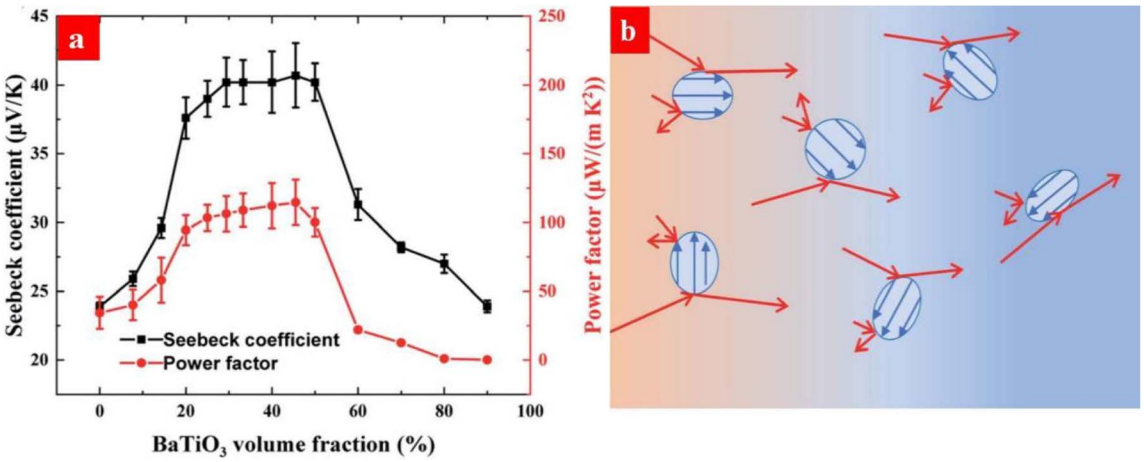

Fig. 15 (a) Changes of the Seebeck coefficient and power factor the of PEDOT:PSS/$BaTiO_3$ films. (b) Schematic diagram of energy filtering of PEDOT:PSS by the ferroelectric $BaTiO_3$ nanoparticles (blue dots). The blue and red arrows are for the spontaneous electric polarization in the $BaTiO_3$ nanoparticles and the hole transport, respectively. The charge carriers migrate from the hot end (red regions) to the cold end (blue regions) under a temperature gradient. Reproduced with permission.[178] Copyright 2021, Royal Society of Chemistry.

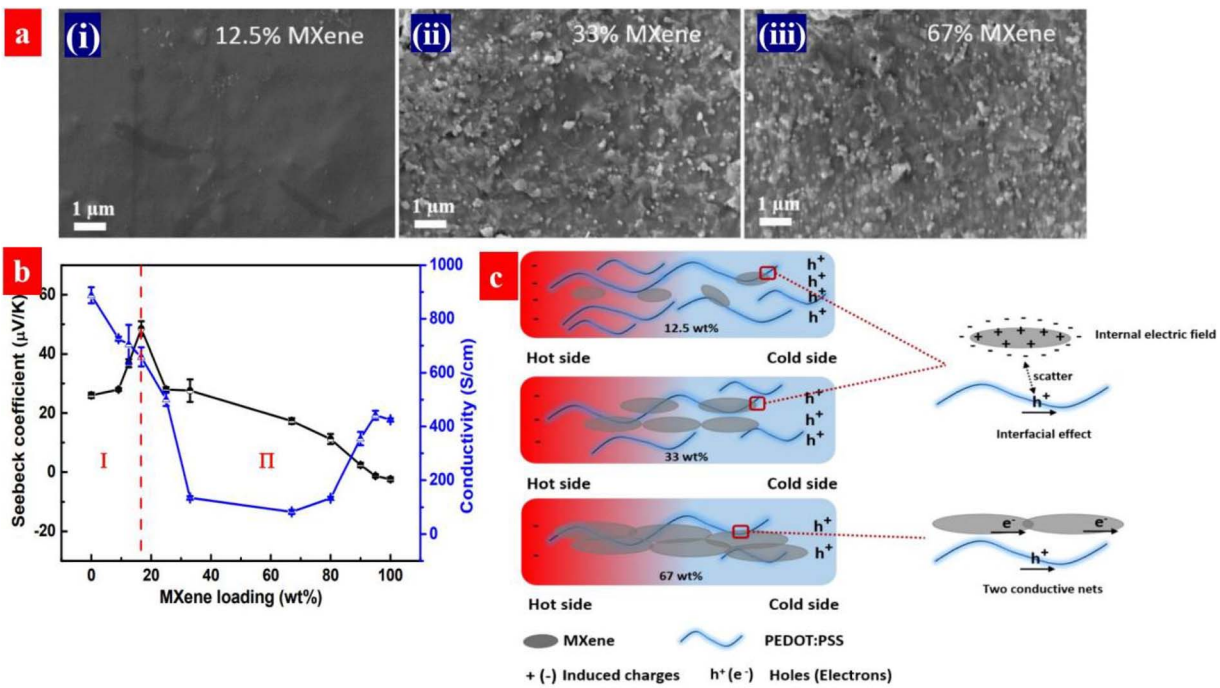

Fig. 16 (a) SEM of the MXene/PEDOT:PSS composites with a different MXene loadings: (i) 12.5 wt%, (ii) 33 wt% and (iii) 67 wt%. (b) Seebeck coefficient and electrical conductivity of the composites as a function of the MXene loading. (c) Schematic illustration for the MXene/PEDOT:PSS interface at the different MXene loadings. Reproduced with permission.[179] Copyright 2020, American Chemical Society.

the Seebeck coefficient is increased, since it depends to E_J and the Fermi level (E_F), $S = (E_F - E_J)/T$.

Energy filtering has been used to improve the thermoelectric properties of PEDOT:PSS. For example, Bi_2Te_3, which serves as a popular inorganic thermoelectric material, was added into PEDOT:PSS.[174] Electron transfer occurs between Bi_2Te_3 and PEDOT:PSS because of their different Fermi levels. It induces the energy filtering for the charge carriers in PEDOT:PSS and thus increases the Seebeck coefficient. Carbon nanotubes (CNTs) were also studied as the fillers of PEDOT:PSS, and this can induce energy filtering and thus increase the Seebeck coefficient.[175–177] Recently, Li *et al.* reported that ferroelectric $BaTiO_3$ nanoparticles could induce energy filtering and thus increased the Seebeck coefficient of PEDOT:PSS from 23.8 to 40.7 μV K^{-1}.[178] The energy filtering is ascribed to the scattering of charge carriers with low energy by the spontaneous electric polarization of $BaTiO_3$ (Fig. 15).

PEDOT:PSS is a p-type thermoelectric polymer. Energy filtering can be induced by forming the composites of PEDOT:PSS and n-type fillers. Guan *et al.* investigated the thermoelectric properties of PEDOT:PSS and MXene ($Ti_3C_2T_x$). The MXene is a n-type 2D material.[179] As shown in Fig. 16, the Seebeck coefficient of the PEDOT:PSS/MXene components is greatly enhanced from 23 to 57.3 μV K^{-1} by the MXene at the loading below 33 wt%. Correspondingly, the power factor is increased from 44.1 to 155 μW m^{-1} K^{-2}. The high thermoelectric performances are attributed to the energy filtering to the electric field at the interface between MXene to PEDOT:PSS due to the electron transfer. However, the Seebeck coefficient decreases with the increase of the MXene loading when the MXene loading exceeds 33 wt%. It should be mentioned that the MXene, as a n-type TE material, can decrease the Seebeck coefficient.

Ouyang *et al.* also observed energy filtering for TE materials coated with a secondary material arising from the scattering of the charge carriers at the surface of the PEDOT:PSS thin films.[180] Energy filtering occurs when the secondary layer is an ionic material or a material with a high intrinsic dipole moment. Under temperature gradient, ions can accumulate at the cold end, the so-called Soret effect.[181] Fan *et al.* observed that coating an ionic liquid layer can greatly increase the Seebeck coefficient of PEDOT:PSS to 70 μV K^{-1} while only slightly lower its conductivity.[182] Inspiringly, the highest power factor is 754 μW m^{-1} K^{-2} for thermoelectric polymers. The surface energy filtering occurred when the PEDOT:PSS thin film is covered with a layer of quasi-solid ionic liquid gel[183] or a layer of polyelectrolyte.[184] Table 4 summarizes the electrical conductivity, Seebeck coefficient and power factor of the thermoelectric devices based on PEDOT:PSS and its components.

Table 4 Thermoelectric performances of TEs with PEDOT:PSS and its components

Material	Method and strategy	σ (S cm^{-1})	S (μV K^{-1})	PF (μW m^{-1} K^{-2})	Ref.	Year
PEDOT:PSS	99 wt% $SClO_2$ treatment	2230	22.8	115.9	96	2022
KPHI/PEDOT:PSS	Two-layer structures under light of 420 nm	1960	39.5	213	173	2022
TiO_2/PEDOT:PSS	Two-layer structures under light of 365 nm	1917	33.3	306	172	2021
PEDOT:PSS:$BaTiO_3$	$BaTiO_3$ nanoparticle components	700	40.7	117	178	2021
PEDOT:PSS/PVA/SWCNT	Drop-casting with IL composites	1800	23.7	106.1	51	2021
PEDOT:PSS:Bi_2Te_3	Bi_2Te_3 nanowires composites	1010	47	223	174	2020
PEDOT:PSS/MXene	Energy filtering by an n-type filler	500	57.3	155	179	2020
PEDOT:PSS	PEIE reduces the evaporation of HNO_3	1580	37.5	168	52	2020
PEDOT:PSS/SWCNT	Physical mixing and DMSO/NaOH treatments	1700	55.6	526	177	2019
PSSH/PEDOT:PSS	Two-layer structures with acid and base treatments	2120	43.5	401	184	2018
PSSNa/PEDOT:PSS	Two-layer structures with acid and base treatments	1732	48.1	401	184	2018
PEDOT:PSS/IL	Acid treatment and energy filtering by IL layer fillers	1580	69	754	182	2018
PEDOT:PSS	MAI solutions in co-solvent of 80 vol% DMF-20 vol% water	1830	28	144	169	2018
PEDOT:PSS	H_2SO_4 and NaOH treatments	2170	39.2	334	170	2017
PEDOT:PSS/Te/SWCNT	Energy filtering by telluride nanorod and SWNT components	139	118	206	50	2017
PEDOT:PSS:SWCNT	SWCNT components	1350	59	464	176	2017
PEDOT:PSS	Addition of DMSO and PEO	1061	38.4	157.4	47	2015
PEDOT:PSS	TSA and hydrazine/DMSO treatments	1647	49.3	318.4	48	2014

6. Stretchable PEDOT:PSS conductors

Stretchable electronics, such as strain sensors, stretchable OSCs/PSCs, organic LEDs/quantum dot LEDs and TEs, are regarded as among the next-generation ubiquitous electronics. Such stretchable devices typically rely on the most commonly

used stretchable conductors, namely PEDOT:PSS.[185–187] Except a good stretchability required by strain sensors, the stretchable conductors should be of high sensitivity to each mechanical deformation, *e.g.*, bending, twisting, and tensile strains; while for a optoelectronic device such as photovoltaic cells and LEDs, the stretchable conductors serve as a stretchable transparent electrode that should have high optoelectrical properties and good durability against cyclic stretching-relaxing and long-term loading. Recently, novel methodologies have been proposed to realize the high-performance stretchable devices based on the PEDOT:PSS.

6.1. Strain sensors

Strain sensors require a key stretchable conductor that affords mechanical deformations for at least 10^4 cycles while still maintaining an initial conductivity in a relaxing status and show a high sensitivity. The sensitivity is known as gauge factor (GF). $GF = (\Delta R/R_o)/\varepsilon$, where $\Delta R/R_o$ is the normalized change in electrical resistance, and ε is the tensile strain of strain sensors. PEDOT:PSS is regarded as the most promising stretchable polymer conductor in epidermal- and implantable sensors, and the PEDOT:PSS-based strain sensors had been widely employed as electronic skins, health monitors, artificial intelligence, food fermentation monitors, *etc.*[188–192]

Fan *et al.* introduced a highly conductive, stretchable and large-size (4.7 cm × 4.7 cm) PEDOT:PSS film.[105] The film was embedded into PDMS elastomers. The strain sensors showed a high sensitivity of 22 at 20% strain. In 2018, Fan *et al.* also demonstrated a strain sensor with a sandwich structure of poly(vinyl) alcohol (PVA)–PEDOT:PSS blends/conductive PEDOT:PSS/PDMS.[103] The devices exhibited a high sensitivity of 110 at 30% strain and stable responses in both stretching–relaxing and long-term loading tests. However, the sensing strains (≤30%) were not high enough for strain sensors. In 2020, He's group made a breakthrough in sensing range and reliability of the strain sensors (Fig. 17).[193] They reported a stretchable strain sensor consisting of Ag nanowires (NWs)

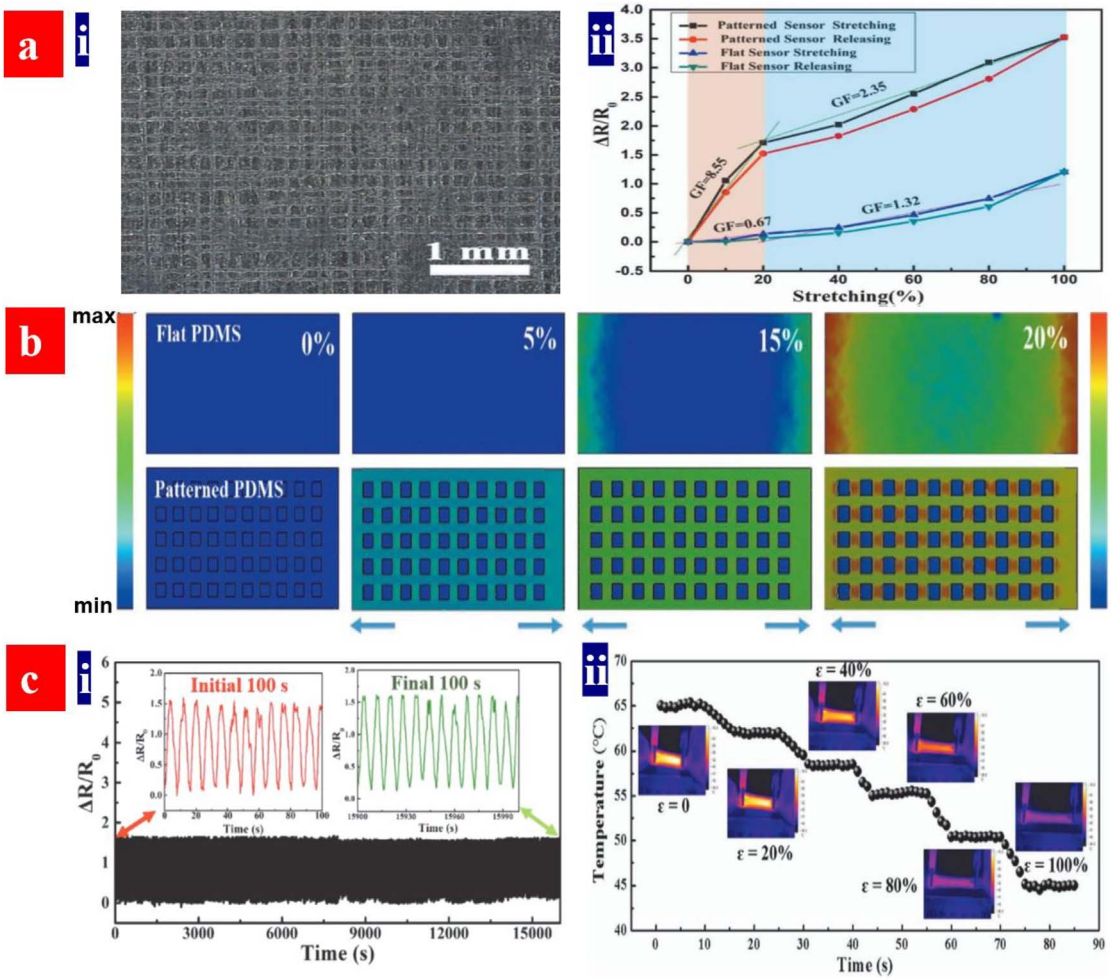

Fig. 17 (a) (i) Optical micrograph of the polyacrylonitrile grids fabricated by near-field electrospinning with a spacing distance (d) of 150 μm, and (ii) relative resistance changes *versus* tensile strains of the strain sensors based on the flat and patterned electrodes. (b) Stress distributions of both flat- and patterned PDMS substrates with $d = 150$ μm during the first straining process. (c) (i) Relative resistance changes *versus* times (1–16000 s) of the sensors under $\varepsilon = 20\%$, and (ii) temperature changes *versus* strains for the strain sensors. Reproduced with permission.[193] Copyright 2020, Wiley-VCH.

and PEDOT:PSS patterned micro-structures. Owing to the micro-structure design of PEDOT:PSS, strong adhesion between PEDOT:PSS and its underlying layers and superior conductivity of Ag NWs, the devices showed a sensitivity of 10.2, a wide sensing range (0–100%), a high reliability for >2000 cycles, and distinct temperature response (31–35 °C). Recently, Xu *et al.* reported free-standing self-powered temperature-strain dual sensors based on PEDOT:PSS/carbon nanocoils (CNCs)–PVA composite films *via* a simple drop casting.[194] The Seebeck coefficient of the PEDOT:PSS/CNC films was 19 μV K^{-1}. This PEDOT:PSS material supplied the thermoelectric powers to detect the temperatures and strains. Under a constant temperature gradient of 30 K, strains from 1% to 10% were detected without any external power supply. The composite films with an array have detected effectively the temperatures of the human's fingers and the motions of the wrist.

Monitoring food processing helps to achieve high quality and high productivity of the food products. In 2021, Ouyang *et al.* demonstrated a strain sensor with biocompatible blends of an intrinsically conducting polymer for real-time monitoring of starch-based food processing (Fig. 18).[86] It monitored the fermentation, steaming, storage and refreshing processed of the food preparation in real time. During fermentation, the volume expansion of the dough with PEDOT:PSS and starches led to an increased resistance; and then the dough volume expanded to the maximum volume that corresponded to the largest resistance. When the resistance becomes stable, the fermentation was finished. The breads with starches and PEDOT:PSS monitored the storage, because volume variation and crevice generation during storage induced a change of the resistances. In the future, it will be revolutionary to invent the multifunctional strain sensors because of the broad applications in human/machine interaction, electronic skins, food production and safety, and wearable sensing electronics.

6.2. Stretchable photovoltaic cells

ITO is an undesirable electrode material in stretchable solar cells owing to its brittleness and low conductivity in a flexing test. Wrinkled and stretchable solar cells were previously realized through spin-coating a PEDOT:PSS transparent electrode on pre-strained PDMS elastomeric substrates[195] or transferring a solar cell foil on pre-strained elastomeric substrates.[196,197] PDMS is one of the most commonly used elastomer substrates in stretchable electronics. However, the PDMS stamps become mechanically robust and tough when stored long-term in ambient air, besides, plenty of large wrinkles and cracks appeared in cyclic stretching-relaxing tests. Therefore, the usage of a soft and durable elastomer as PDMS alternatives is critical for the PEDOT:PSS electrodes and the integrated stretchable devices.

Chen *et al.* demonstrated a stretchable OSC based on PEDOT:PSS transparent electrodes.[198] The PEDOT:PSS aqueous solutions, which contained 5 vol% DMSO and 10 vol% of Zonyl fluorosurfactant, were stirred overnight prior to use. Then, the PEDOT:PSS electrodes were coated on elastomeric substrates of PDMS and 3M VHB 4905 tape (3M tape), respectively. This 3M tape involving modified acrylic molecules did have a high elasticity and viscoelasticity with a large impact force absorption, and the tape provided a weather resistance. On the basis of the structure of 3M tapes/PEDOT:PSS electrodes/PTB7:PC_{71}BM/

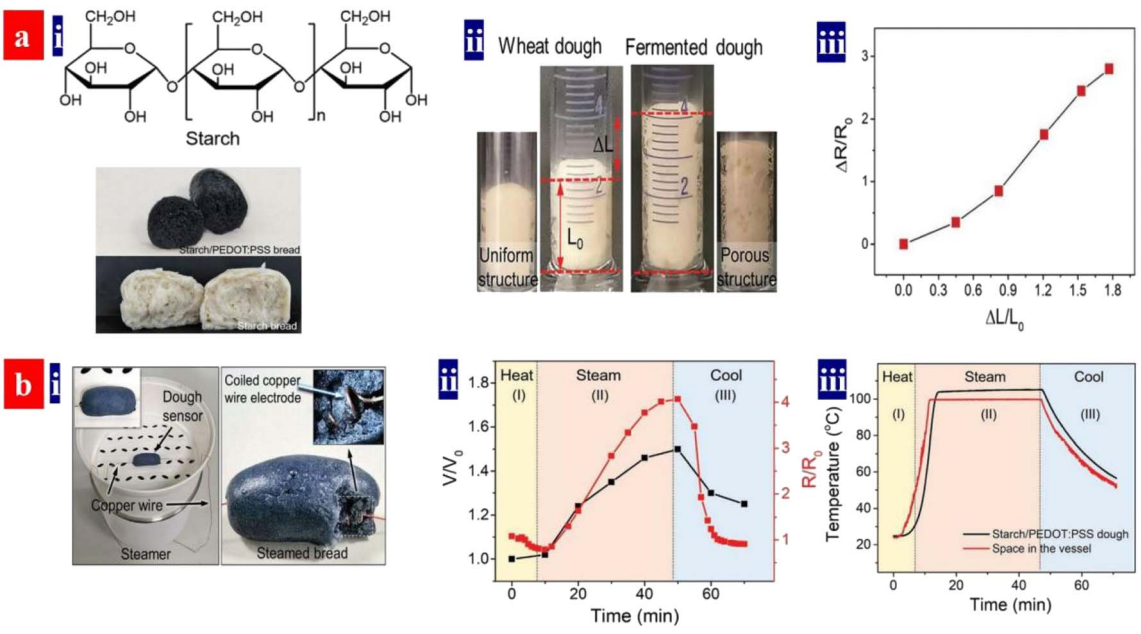

Fig. 18 (a) (i) Molecular structure of starch and photographs of a starch bread involving PEDOT:PSS and as-cast starch breads. (ii) A starch/PEDOT:PSS dough showing a volume expansion in the fermentation. (iii) Resistance variation *versus* length variation of the dough. $R_{initial} = 78$ kΩ, $L_{initial} = 1.5$ cm. (b) (i) Photographs of the setup and a starch/PEDOT bread. (ii) Resistance ($R/R_{initial}$) and volume ($V/V_{initial}$) changes of the dough in the steaming process. $R_{initial} = 75$ kΩ, $V_{initial} = 1.5$ cm^3. (iii) Real-time temperatures of the dough during steaming. Reproduced with permission.[86] Copyright 2021, Wiley-VCH.

eutecticgallium–indium (EGaIn), the stretchable OSCs showed a PCE of 5.2% under illumination of AM1.5 solar simulator (Fig. 19). This PCE is 30% higher than that of the stretchable devices fabricated onto pre-strained PDMS substrates. The raised PCE is due to the favorable surface status of the PEDOT:PSS/3M tapes with small and dense wrinkles that can provide a better interface for the deposition of active layers. Besides, the OSCs had an excellent mechanical stability, maintaining 80% of its original PCE at 20% strain for 50 cycles. Despite the moderate PCE (5.2%) of the stretchable devices, the

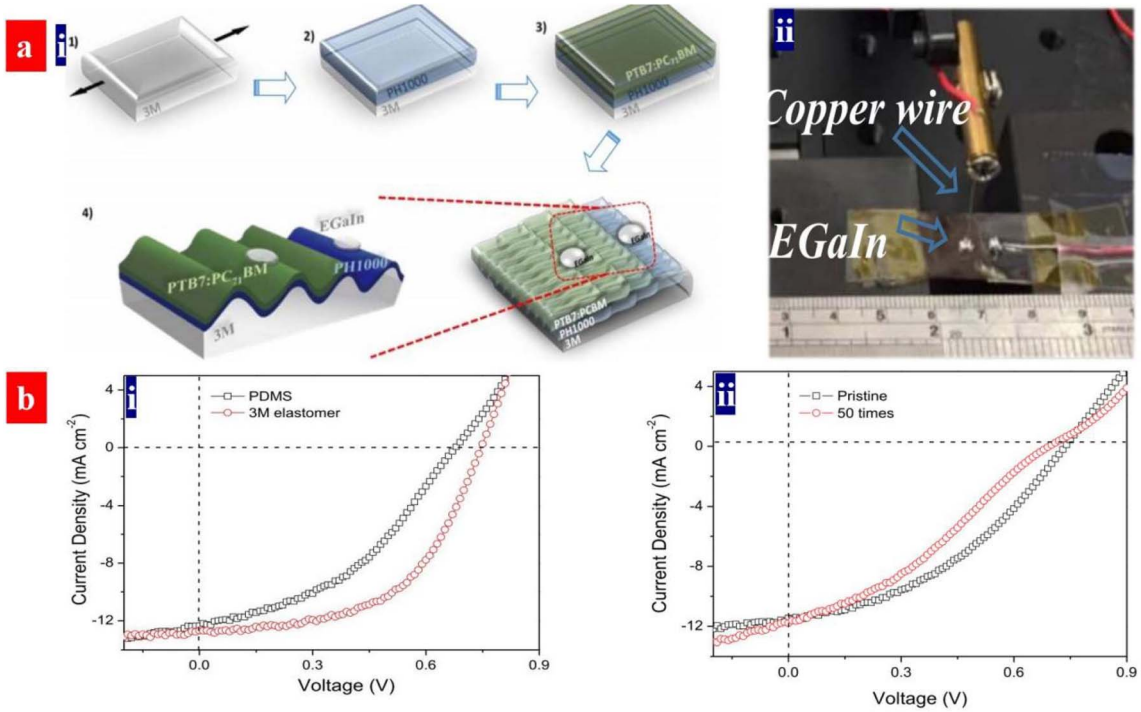

Fig. 19 (a) (i) Illustration of the fabrication process of stretchable OSCs ((1) pre-strain and attachment to glass substrates, (2) spin-coating of PEDOT:PSS, (3) spin-coating of active layers, and (4) removal of the glass and relaxation of the pre-strain), and (ii) images of the solar cell and characterization system. (b) (i) J–V curves of the stretchable OSCs fabricated on PDMS and 3M tapes, and (ii) J–V curves of the stretchable OSCs before and after stretching at 20% strain for 50 cycles. Reproduced with permission.[198] Copyright 2017, Elsevier.

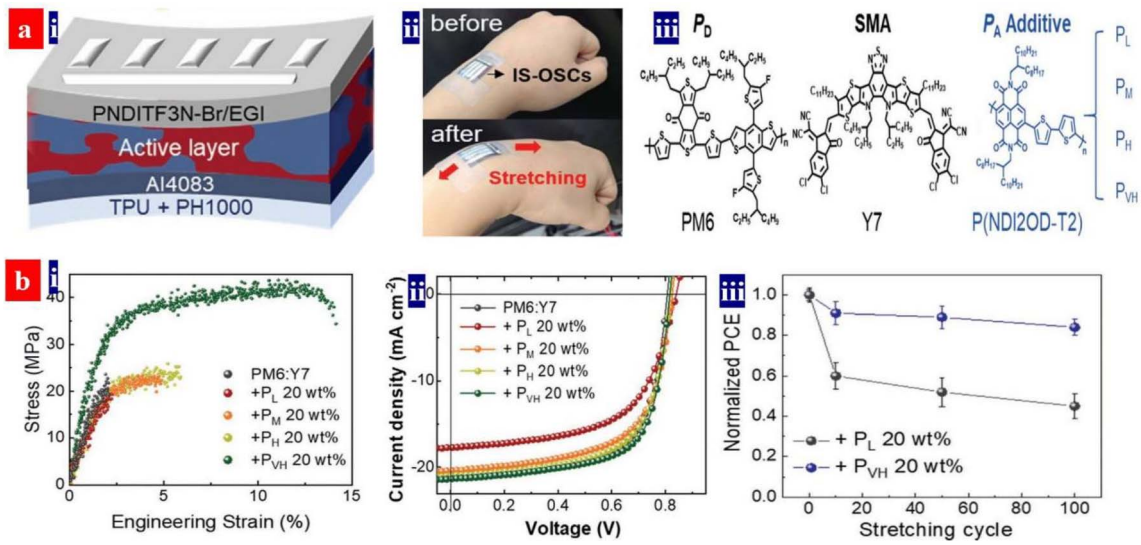

Fig. 20 (a) (i) Stretchable OSC structure, (ii) photographs, and (iii) molecular structures of the PA additives. (b) (i) Stress–strain curves of PM6:Y7 with 20 wt% of PAs of different M_Ws, (ii) J–V curves of the stretchable OSCs as functions of PAs with different M_W, and (iii) normalized PCE curves of the stretchable devices in the flexing tests. Reproduced with permission.[199] Copyright 2022, Wiley-VCH.

PCE will be improved further *via* increasing the electrode conductivity, inserting a buffer layer, and using more efficient ternary active layers.

Organic solar cells (OSCs) can be made as an intrinsically stretchable power source *via* PEDOT:PSS electrode and HTL modifications and a blending strategy of active layers. In 2022, Lee *et al.* demonstrated an intrinsically stretchable OSC that exhibited a high PCE and excellent stretchability (Fig. 20).[199] The device configuration is illustrated as follows: thermoplastic polyurethane (PU) substrates/modified PEDOT:PSS (PH1000) electrodes/modified PEDOT:PSS (P VP AI 4083) HTLs/active layers/PNDIT-F3N-Br/EGaIn. 5 vol% dimethyl sulfoxide (DMSO) was used to increase the electrical conductivity of the PH1000 electrodes; 2 vol% polyethylene glycol (PEG) was employed to prolong the elongation of the PH1000 electrodes; and 0.5 vol% Zonyl fluorosurfactant FS-300 was blended to improve the surface wettability of the P VP AI 4083 HTLs. The mechanically robust active layers were constructed *via* the addition of a high-molecular weight (M_W: 408 kg mol^{-1}) polymer acceptor (PA) to PM6:Y7 active layers. Because the long PA chains served as molecular bridges between different domains and dissipated mechanical stresses for charge transport, high-M_W PA addition could boost the stretchability and PCE of the photovoltaic cells with 20 wt% PA. The stretchable solar cells yielded a high PCE of 11.7% and the devices retained 84% of the initial PCE in a cyclic stretching-releasing test for 100 cycles at 15% strain.

A stretchable active layer of OSCs was also obtained recently *via* usage of a polymer donor (PBB1-Cl) as the third component.[200] It regulated the morphology and molecular accumulation of PM6:Y6-Bo-4Cl active layers. After the addition of 20% PBB1-Cl, the tensile strength and elongation at the break of the ternary blend layers increased from 2.00 to 9.12 N and from 5.83% to 26.86%, respectively. The long elongation is attributed to a formation of a better intertwined and ordered intermolecular stacking in the ternary blends. Li's group compared the mechanical properties of several representative active layers of organic solar cells.[201,202] Among the active layers, the PM6:PC_{60}BM films had the maximum crack-onset strain of 4.58% and the highest toughness of 169.47 J cm^{-3}.[201] We envision that the PM6:PC_{60}BM active layers which were blended with a third component are suitable to fabricate more efficient and mechanically robust OSCs based on stretchable PEDOT:PSS electrodes. There is a high probability that this ternary active layer blend will allow for the creation of stretchable photovoltaic cells that can show a high PCE of over 15% along with a large tensile strain over 25%.

6.3. Intrinsically stretchable PLEDs

A wrinkled configuration of optoelectronics is not considered to be intrinsically stretchable. Intrinsically stretchable optoelectronics require that all of the components (underlying substrates, photoactive layers, both electrodes sandwiched the active layers, and buffer layers) are intrinsically stretchable. Such unprecedented devices on skin-like underlying substrates should be highly soft, intrinsically stretchable and highly efficient.[203–207] Intrinsically stretchable polymer materials have the promise of good strain tolerance.[208,209] However, it has been very challenging to invent these kinds of intrinsically stretchable solar cells and LEDs with considerably high efficiency.

Inspiringly, Bao's group recently demonstrated a stretchable all-polymer LED that comprised a stretchable anode of PEDOT:PSS blended with polyrotaxane (PR) and a hole injection layer of PEDOT:PSS/Triton X (8 nm).[210] This PR is a cross-linking agent and it forms from PEG and α-cyclodextrin (α-CD), exhibiting free movement of the cyclic α-CD along the linear PEG.[211,212] A resultant three-dimensional (3D) network was prepared with the PR agents.[213] Here, the anode (150 nm) was spin-coated on a soft substrate of PVDF-HFP (100 μm), and a stretchable light-emitting layer of Super Yellow (SY) with polyurethane was innovatively employed. The resultant all-polymer-based LED yielded a high brightness of 7450 cd m^{-2}, current efficiency of 5.3 cd A^{-1}, and stretchability of up to 100% strain. The work showed an advancement towards high-performance intrinsically stretchable LEDs, and it improved visual human–electronic interfaces for stretchable displays.

However, doping treatments and engineering strategies to making elastic and durable transparent electrodes are emergent and significant for the development of the intrinsically stretchable optoelectronics. Brightness, current efficiency, tensile strains, durability and operation lifetimes should be raised further in the next-generation LEDs. Besides, the device durability should be investigated in at least 10^4 stretching-relaxing tests at a strain no lower than 30% and long-time (*e.g.*, 5 min) loading tests for a true adaptation of the lighting and display products.

6.4. Stretchable thermoelectrics

The development of stretchable and power-supply systems has the advantages of lightweight, wearability, self-sustaining and high compatibility with human skins.[5,97,214–218] However, the usage of as-cast PEDOT:PSS films is currently constrained by their intrinsic small elongation of <2.0%. An elastomer blending strategy was commonly used to raise the mechanical property, while DMSO and ionic liquids were generally employed to raise the electrical conductivity of the PEDOT:PSS materials.

In 2018, Taroni *et al.* showed a tough and processable self-standing film based on PEDOT:PSS and commercial elastomeric polyurethane (Lycra) blends.[219] The PEDOT:PSS (Clevios PH1000) was freeze dried, and then dispersed into DMSO followed by a probing sonication. An unprecedented strain at break of 700 ± 150% was reached for the TEs with a blend containing 90 wt% Lycra. After EG bath, the thermoelectric films showed an electrical conductivity of 79 S cm^{-1} and a Seebeck coefficient of 16 μV K^{-1}. Subsequently, in 2020, Ouyang *et al.*[84] prepared a stretchable and transparent ionogel with high thermoelectric properties *via* a drop-casting method (Fig. 21). The ionogels made of waterborne polyurethane (WPU) and 1-ethyl-3-methylimidazolium dicyanamide (EMIM:DCA). The ionogels with 40 wt% EMIM:DCA possessed a superior stretchability of up to 156%, a low tensile strength of 0.6 MPa,

and a low Young's modulus of 0.6 MPa. The stretchable ionogels exhibited a high ionic thermovoltage of 34.5 mV K^{-1} along with a high ionic conductivity of 8.4 mS cm^{-1}.

In 2021, Wen *et al.* realized a stretchable TE fiber that consisted of PEDOT:PSS and WPU and ionic liquids of 1-ethyl-3-methylimidazolium tricyanomethanide (EMIM TCM) *via* using one-step wet-spinning approach (Fig. 22).[220] In the PEDOT:PSS/WPU composite fibers, WPU not only acts as an elastomeric matrix, but also it has a template effect on (i) improving the packing order and (ii) increasing the linearity of the PEDOT chains during wet-spinning. 10 wt% EMIM TCM composites were added to the PEDOT:PSS aqueous solution to raise the electrical conductivity. The composite fibers showed a desirable wearable merit and a power factor of

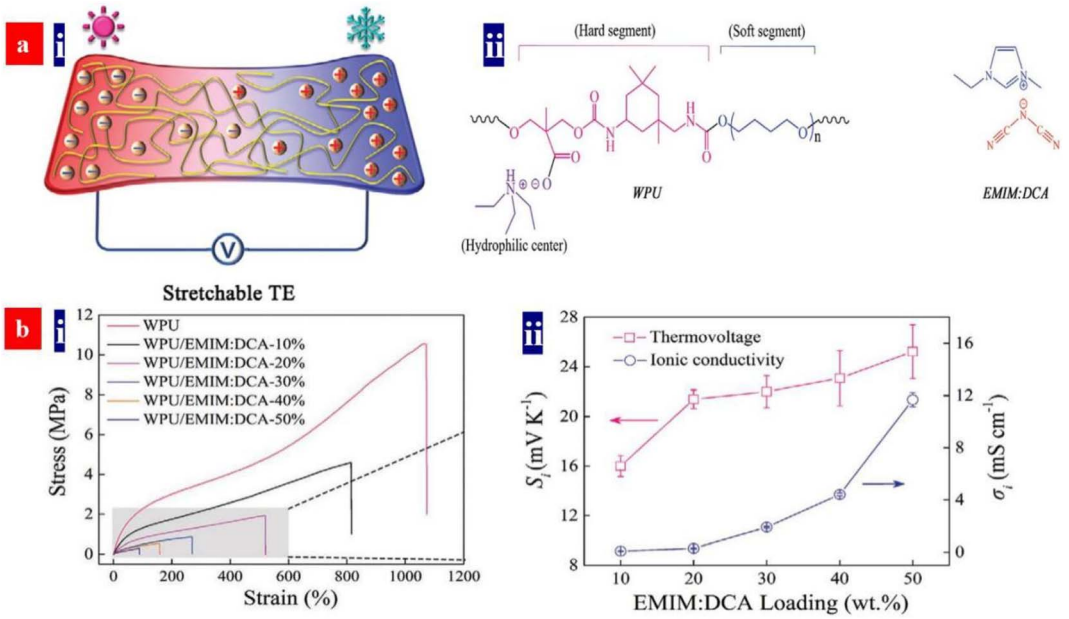

Fig. 21 (a) Schematic diagram of device operation, and chemical structures of WPU and EMIM:DCA. (b) (i) Stress–strain characteristics of the WPU film and WPU/EMIM:DCA ionogels; and (ii) profiles of thermovoltage and ionic conductivity of WPU/EMIM:DCA ionogels with various EMIM:DCA loading. Reproduced with permission.[84] Copyright 2020, Wiley-VCH.

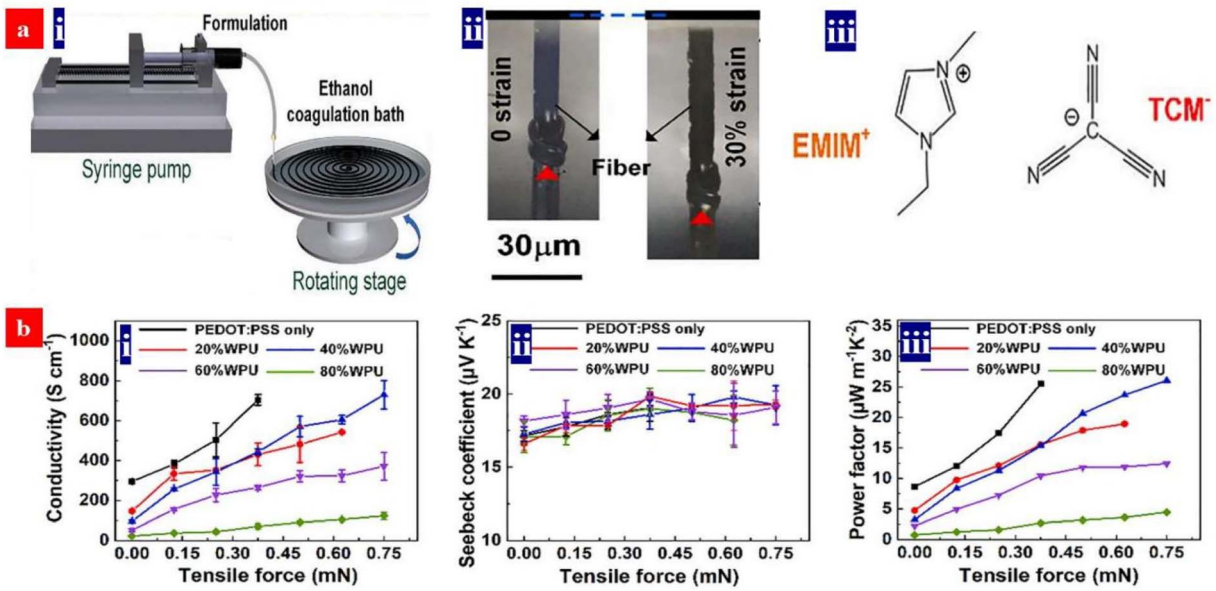

Fig. 22 (a) (i) Schematic diagram of the wet-spinning fabrication of PEDOT:PSS/WPU composite fibers; (ii) photographs of the composite fibers blended with EMIM:TCM at relaxing and stretching states; and (iii) molecular structure of EMIM:TCM. (b) Dependences of electrical conductivity (i) Seebeck coefficient (ii) and PF (iii) of the PEDOT:PSS fiber and the composite fibers under different tensile loading with the tensile forces of 0, 0.125, 0.25, 0.375, 0.5, 0.625 and 0.75 mN, respectively. Reproduced with permission.[220] Copyright 2021, Elsevier.

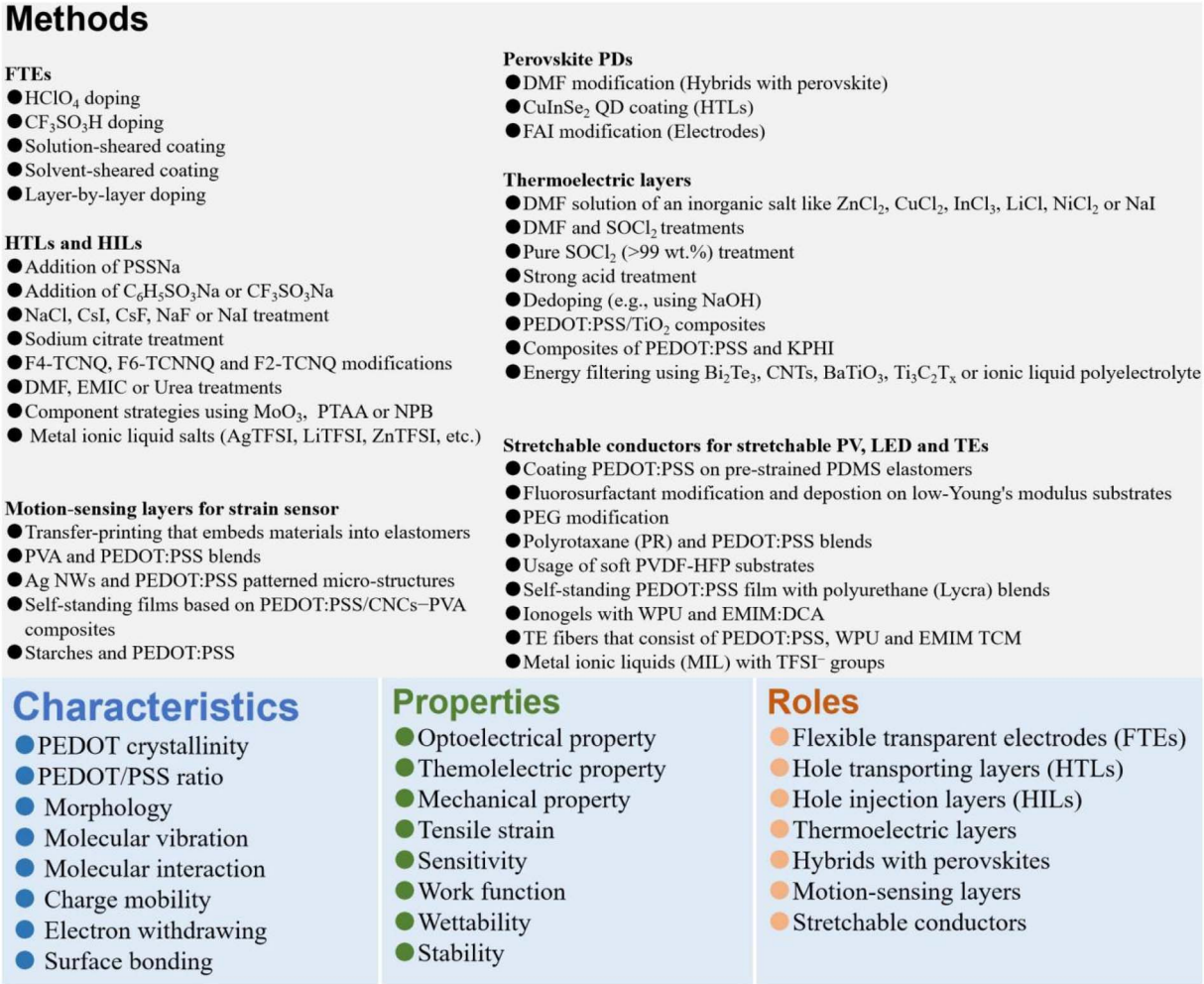

Fig. 23 Schematic diagrams of the methods that adjust the film characteristics and properties and lead to the key roles played in the various optoelectronic, thermoelectric, and flexible and stretchable devices.

26.1 μW m K^{-2}. The resultant PEDOT:PSS/WPU composite fibers not only possessed a good intrinsic stretchability with an elongation-at-break of >30%, but they also exhibited an excellent performance stability and self-recoverability in cyclic stretching tests.

In the future, we suggest that metal ionic liquids (MIL) with $TFSI^-$ groups, strong acids, and bases are used to balance the electrical conductivity, Seebeck coefficient and operation stability of the TE fibers. The reasons are obvious, such as the superior conductivity of the strong acid-treated PEDOT:PSS films,[94,99] a potentially high stability of the devices based on the MIL-treated PEDOT:PSS films,[91] and the dedoping effect induced by the bases (*e.g.*, NaOH[170]). Notably, the strong acid doping should be suitable to the composite fibers through substantially reducing the doping temperatures and dopant concentrations. This gentle acid approach can avoid a chemical corrosion of strong acids to most of underlying plastic substrates and the elastomers involving WPU. Therefore, a highly thermoelectric, stable and stretchable TE based on PEDOT:PSS can be realized and it's promising for wearable and portable energy supply.

7. Conclusion and outlook

State-of-the-art approaches and methodologies were reviewed and proposed to raise the optoelectrical properties, work function, thermoelectric properties, stretchability, wettability and stability of the PEDOT:PSS films and stretchable conductors. As displayed in Fig. 23, the latest innovative methods include: (i) CF_3SO_3H doping, $HClO_4$ doping, solution shearing, solvent shearing, and layer-by-layer treatments for the electrode preparations; (ii) sulfonate, sodium salt, cesium salt, F4-TCNQ, DMF, ionic liquids and urea treatments and component strategies using NPB, PTAA, PANI-phenoxazine and MoO_3 for the HTL preparations; (iii) secondary solvent treatments, strong acid doping, $SClO_2$ doping, energy-filtering methodologies, n-type TE composites and dedoping for the TE layer realizations; (iv) soft material blending, underlying substrate selection methodologies, and ionogel formulation for the stretchable conductor realizations; and (v) elastomeric blends and freeze drying for the stretchable TE fabrications. There has been much intensive research and significant progress on optoelectronics and thermoelectrics with the multifunctional PEDOT:PSS

materials. Nevertheless, there are still major challenges and shortcomings to overcome that have negative impact on the development of related devices fabricated from PEDOT:PSS-based materials. Many insightful suggestions for success towards such necessary achievements are provided below.

First, these modification treatments and film-deposition-processing approaches not only raise the electrical conductivity, work function, stretchability, and wettability of the resultant PEDOT:PSS films, but perovskite layers fabricated on top of these films are also induced into the formation of large grain sizes, less defects, and overall higher crystallinity. It is advised that both modification treatments and processing approaches for PEDOT:PSS films should be organically combined, meaning that both modification methods and processing approaches should be universal and suitable to various kinds of devices towards higher performance. Additionally, a combined treatment has a higher probability of further promoting charge transfer into PEDOT:PSS matrices while synergistically improving film properties. Thus, it is believed that such will pave an avenue to enhance the performances and prolong the operational lifetimes of corresponding solar cells, LEDs, PPDs, TEs, strain sensors, and flexible and stretchable electronics.

Then, there are several concerns that should be openly considered with regards to electrode fabrication and implementation. (i) There is currently no route to obtain PEDOT:PSS electrodes with a high enough conductivity comparable to those of commercial ITO electrodes or Ag nanowire electrodes. It has been found that a better morphology with refined PEDOT-rich nanoparticles and nanofibrils can largely improve the electrical conductivity.[94] Thus, new methods to improve film morphology as well crystallinity should be continuously pursued. (ii) There are few studies that formulate links between PEDOT:PSS film overall stability and related device performance. Overall PEDOT:PSS stability includes electrical, electrochemical, work function, structural, and morphological stability against ambient air, UV light, and relatively high temperatures. Although PEDOT:PSS can exhibit a raised stability and a good conductivity, they aren't optimal for high-performance electronic devices. In order to make stabilized PEDOT:PSS films; PEDOT crystallinity, electronic structure, PEDOT/PSS ratio, molecular interactions, surface hydrophobicity, and interfacial adhesion should be considered together and optimized concurrently. (iii) Micro-patterned PEDOT:PSS films (or PEDOT:PSS pixels) are desirable for broad applications in solar cells, high-resolution micro-displays, touch sensors, and flexible and stretchable electronics. Advanced photolithography and plasma-etching techniques will be required for future realization of micro-patterned films and high-resolution PEDOT:PSS pixels.

Next, sulfonate groups, dopant molecules, and metal ion dopants can potentially migrate towards, diffuse into, and potentially poison other active components of PSC devices, leading to detrimental reactions and poor photovoltaic performance. Indeed, the underlying mechanisms of device-performance degradation and failure modes are somewhat ambiguous. In order to improve the photovoltaic performance, one method is to use unique dopants involving fluorochlorine polar molecular bonds and hydrophilic groups. The use of these dopants has the advantages of improving the work function of the PEDOT:PSS thin films, inducing more seamless contact at interfaces, reducing the sulfonate levels in matrices, and inducing higher crystallinity of subsequent perovskite layers. It will also induce shorter charge transport times and higher charge carrier lifetimes for these PSCs. Another method is to employ an interfacial shield with a chemically stable metal oxide layer (*e.g.*, MoO_3, NiO_x, or Al_2O_3). Such shielding treatments using inert metal oxides is also favorable for improving charge-carrier transport and hole extraction.

Finally, an improved encapsulation is critical to promote the stability of these optoelectronic devices. The PEDOT:PSS material is intrinsically sensitive to moisture and oxygen, which can degrade its optoelectrical properties over time. It is challenging to fully avoid the permeation of water and oxygen from ambient air into devices. Researchers explored different strategies to improve the stability of the optoelectronic devices *via* using self-encapsulating nucleation layers[221] and plasma-enhanced molecular layer deposition,[222] to ensure long-term functionality and reliability of these devices. Besides, two-dimensional materials such as graphene and Ti_3C_2 (MXene) can restrain the penetration of water and oxygen into devices. Thus, a blend of standard packaging materials with such two-dimensional materials has a high probability of improving device stability. Another possibility is to employ an encapsulation film, *e.g.*, an organic film sandwiched with a stable metal oxide film (SiN_x, SiO_2, $SiO_{1-x}N_x$, Al_2O_3, or ZrO_2), which is one of the best options for device packaging. These metal oxide films are usually prepared through using low-temperature plasma enhanced chemical vapor deposition or atomic layer deposition. Notably, for curved devices, an inorganic-organic-inorganic (IOI) encapsulation film with a total of 8 to 10 μm thickness is suggested; whereas, for flexible and stretchable devices, an IOI encapsulation layer with a total of 1 to 2 μm thickness is advised for employment. Indeed, these packaging materials and encapsulation technologies are critical for an adaptation of curved, flexible, and stretchable optoelectronics and thermoelectrics. It is hoped that by means of the aforementioned methods, scientists and engineers can collaborate together for a brighter future of these OSCs, PSCs, LEDs, PPDs, TEs, touch sensors, and flexible and stretchable devices based on PEDOT:PSS materials.

Conflicts of interest

There are no conflicts to declare.

Acknowledgements

We are grateful for financial support from the Ningbo Natural Science Foundation (2021J195), and Zhejiang Provincial Natural Science Foundation of China under Grant no. LGG22F040003.

Notes and references

1 C. Z. Liao, C. H. Mak, M. Zhang, H. L. W. Chan and F. Yan, *Adv. Mater.*, 2015, **27**, 676.

2 H. Huang, Y. Zhao, T. Cong, C. Li, N. Wen, X. Zuo, Y. Guo, H. Zhang, Z. Fan and L. Pan, *Adv. Funct. Mater.*, 2022, **32**, 2110777.
3 B. J. Worfolk, S. C. Andrews, S. Park, J. Reinspach, N. Liu, M. F. Toney, S. C. B. Mannsfeld and Z. N. Bao, *Proc. Natl. Acad. Sci. USA*, 2015, **112**, 14138.
4 Y. Qi, M. Almtiri, H. Giri, S. Jha, G. Ma, A.-K. Shaik, Q. Zhang, N. Pradhan, X. Gu, N.-I. Hammer, D. Patton, C. Scott and Q. Dai, *Adv. Energy Mater.*, 2022, **12**, 2202713.
5 M. Abarkan, A. Pirog, D. Mafilaza, G. Pathak, G. N'Kaoua, E. Puginier, R. O'Connor, M. Raoux, M. J. Donahue, S. Renaud and J. Lang, *Adv. Sci.*, 2022, **9**, 2105211.
6 S. Gong and W. L. Cheng, *Adv. Electron. Mater.*, 2017, **3**, 1600314.
7 J. Lu, W. Feng, G. Mei, J. Sun, C. Yan, D. Zhang, K. Lin, D. Wu, K. Wang and Z. Wei, *Adv. Sci.*, 2020, **7**, 2000689.
8 Y. Wang, C. X. Zhu, R. Pfattner, H. P. Yan, L. H. Jin, S. C. Chen, F. Molina-Lopez, F. Lissel, J. Liu, N. I. Rabiah, Z. Chen, J. W. Chung, C. Linder, M. F. Toney, B. Murmann and Z. N. Bao, *Sci. Adv.*, 2017, **3**, e1602076.
9 X. T. Hu, X. C. Meng, L. Zhang, Y. Y. Zhang, Z. R. Cai, Z. Q. Huang, M. Su, Y. Wang, M. Z. Li, F. Y. Li, X. Yao, F. Y. Wang, W. Ma, Y. W. Chen and Y. L. Song, *Joule*, 2019, **3**, 2205–2218.
10 Y. Cui, F. Zhang, G. Chen, L. Yao, N. Zhang, Z. Liu, Q. Li, F. Zhang, Z. Cui, K. Zhang, P. Li, Y. Cheng, S. Zhang and X. Chen, *Adv. Mater.*, 2021, **33**, 2100221.
11 D. H. Kim, J. H. Ahn, W. Mook Choi, H. S. Kim, T. H. Kim, J. Song, Y. Y. Huang, Z. Liu, C. Lu and J. A. Rogers, *Science*, 2008, **320**, 507.
12 D. J. Lipomi, M. Vosgueritchian, B. C. Tee, S. L. Hellstrom, J. A. Lee, C. H. Fox and Z. Bao, *Nat. Nanotechnol.*, 2011, **6**, 788.
13 M. L. Hammock, A. Chortos, B. C.-K. Tee, J. B.-H. Tok and Z. Bao, *Adv. Mater.*, 2013, **25**, 5997.
14 T. Someya, Z. Bao and G. G. Malliaras, *Nature*, 2016, **540**, 379.
15 D. Son, J. Lee, S. Qiao, R. Ghaffari, J. Kim, J. E. Lee, C. Song, S. J. Kim, D. J. Lee, S. W. Jun, S. Yang, M. Park, J. Shin, K. Do, M. Lee, K. Kang, C. S. Hwang, N. Lu, T. Hyeon and D.-H. Kim, *Nat. Nanotechnol.*, 2014, **9**, 397.
16 D. H. Kim and Y. Lee, *Nat. Nanotechnol.*, 2015, **10**, 570.
17 I. R. Minev, P. Musienko, A. Hirsch, Q. Barraud, N. Wenger, E. M. Moraud, J. Gandar, M. Capogrosso, T. Milekovic, L. Asboth, R. F. Torres, N. Vachicouras, Q. Liu, N. Pavlova, S. Duis, A. Larmagnac, J. Voeroes, S. Micera, Z. Suo, G. Courtine and S. P. Lacour, *Science*, 2015, **347**, 159.
18 Y. B. Cheng, A. Pascoe, F. Huang and Y. Peng, *Nature*, 2016, **539**, 488.
19 G. Zeng, W. Chen, X. Chen, Y. Hu, Y. Chen, B. Zhang, H. Chen, W. Sun, Y. Shen, Y. Li, F. Yan and Y. Li, *J. Am. Chem. Soc.*, 2022, **144**, 8658–8668.
20 D. J. Lipomi and Z. Bao, *MRS Bull.*, 2017, **42**, 93.
21 J. R. Tumbleston, B. A. Collins, L. Yang, A. C. Stuart, E. Gann, W. Ma, W. You and H. Ade, *Nat. Photonics*, 2014, **8**, 385.
22 H. Kang, S. Jung, S. Jeong, G. Kim and K. Lee, *Nat. Commun.*, 2015, **6**, 6503.
23 J. Tong, S. Xiong, Y. Zhou, L. Mao, X. Min, Z. Li, F. Jiang, W. Meng, F. Qin, T. Liu, R. Ge, C. Fuentes-Hernandez, B. Kippelen and Y. Zhou, *Mater. Horiz.*, 2016, **3**, 452.
24 S. I. Na, S. S. Kim, J. Jo and D. Y. Kim, *Adv. Mater.*, 2008, **20**, 4061.
25 T. Liu, L. Sun, X. Dong, Y. Jiang, W. Wang, C. Xie, W. Zeng, Y. Liu, F. Qin, L. Hu and Y. Zhou, *Adv. Funct. Mater.*, 2021, **31**, 2107250.
26 T. Y. Qu, L. J. Zuo, J. D. Chen, X. L. Shi, T. Zhang, L. Li, K. C. Shen, H. Ren, S. Wang, F. M. Xie, Y. Q. Li, A. K. Y. Jen and J. X. Tang, *Adv. Opt. Mater.*, 2020, **8**, 2000669.
27 D. Koo, S. Jung, J. Seo, G. Jeong, Y. Choi, J. Lee, S. M. Lee, Y. Cho, M. Jeong, J. Lee, J. Oh, C. Yang and H. Park, *Joule*, 2020, **4**, 1021.
28 X. Zheng, L. Zuo, F. Zhao, Y. Li, T. Chen, S. Shan, K. Yan, Y. Pan, B. Xu, C.-Z. Li, M. Shi, J. Hou and H. Chen, *Adv. Mater.*, 2022, **34**, 2200044.
29 W. S. Yang, J. H. Noh, N. J. Jeon, Y. C. Kim, S. Ryu, J. Seo and S. I. Seok, *Science*, 2015, **348**, 1234.
30 G. Yang, C. Chen, F. Yao, Z. L. Chen, Q. Zhang, X. L. Zheng, J. J. Ma, H. W. Lei, P. L. Qin, L. B. Xiong, W. J. Ke, G. Li, Y. F. Yan and G. J. Fang, *Adv. Mater.*, 2018, **30**, 1706023.
31 D. Yang, R. Yang, J. Zhang, Z. Yang, S. Liu and C. Li, *Energy Environ. Sci.*, 2015, **8**, 3208.
32 H. Yu, Y. Xie, J. Zhang, J. Duan, X. Chen, Y. Liang, K. Wang and L. Xu, *Adv. Sci.*, 2021, **8**, 2004510.
33 Z. Wang, L. Zeng, C. Zhang, Y. Lu, S. Qiu, C. Wang, C. Liu, L. Pan, S. Wu, J. Hu, G. Liang, P. Fan, H.-J. Egelhaaf, C. J. Brabec, F. Guo and Y. Mai, *Adv. Funct. Mater.*, 2020, **30**, 2001240.
34 P. Lin, W. Zhang, L. Tian, L. Jia, F. Wen, G. Duan, X. Zhou, S. Zhou, F. Zhang, Y. Jiang, T. Chen, F. Liu, S. Yang and Y. Huang, *ACS Appl. Energy Mater.*, 2021, **4**, 4408–4415.
35 C. K. Liu, H. L. Loi, J. Cao, G. Tang, F. Liu, Q. Huang, X. Liang and F. Yan, *Small Struct.*, 2021, **2**, 2000084.
36 C. Xie, C.-K. Liu, H.-L. Loi and F. Yan, *Adv. Funct. Mater.*, 2020, **30**, 1903907.
37 J.-Y. Lin, F.-C. Hsu, C.-Y. Chang and Y.-F. Chen, *J. Mater. Chem. C*, 2021, **9**, 5190–5197.
38 X. Du, W. Tian, J. Pan, B. Hui, J. Sun, K. Zhang and Y. Xia, *Nano Energy*, 2022, **92**, 106694.
39 F. P. G. de Arquer, A. Armin, P. Meredith and E. H. Sargent, *Nat. Rev. Mater.*, 2017, **2**, 16100.
40 L. Dou, Y. M. Yang, J. You, Z. Hong, W.-H. Chang, G. Li and Y. Yang, *Nat. Commun.*, 2014, **5**, 5404.
41 Q. J. Sun, Y. A. Wang, L. S. Li, D. Wang, T. Zhu, J. Xu, C. H. Yang and Y. F. Li, *Nat. Photonics*, 2007, **1**, 717.
42 K. Goushi, K. Yoshida, K. Sato and C. Adachi, *Nat. Photonics*, 2012, **6**, 253.
43 X. L. Dai, Z. X. Zhang, Y. Z. Jin, Y. Niu, H. J. Cao, X. Y. Liang, L. W. Chen, J. P. Wang and X. G. Peng, *Nature*, 2014, **515**, 96.
44 H. Nakanotani, T. Higuchi, T. Furukawa, K. Masui, K. Morimoto, M. Numata, H. Tanaka, Y. Sagara, T. Yasuda and C. Adachi, *Nat. Commun.*, 2014, **5**, 4016.

45 A. Islam, J. Li, M. Pervaiz, Z.-H. Lu, M. Sain, L. Chen and X. Ouyang, *Adv. Energy Mater.*, 2019, **9**, 1803354.
46 S. H. Yoon, D. Gwak, H. H. Kim, H. J. Woo, J. Cho, J. W. Choi, W. K. Choi, Y. J. Song, C.-L. Lee, J. Park, K. Heo and Y. J. Choi, *ACS Photonics*, 2019, **6**, 743–748.
47 C. Yi, A. Wilhite, L. Zhang, R. Hu, S. S. C. Chuang, J. Zheng and X. Gong, *ACS Appl. Mater. Interfaces*, 2015, **7**, 8984.
48 K. Jiang, S.-H. Hong, S.-H. Tung and C.-L. Liu, *J. Mater. Chem. A*, 2022, **10**, 18792.
49 Q. K. Li, M. J. Deng, S. M. Zhang, D. K. Zhao, Q. L. Jiang, C. F. Guo, Q. Zhou and W. S. Liu, *J. Mater. Chem. C*, 2019, **7**, 4374.
50 E. J. Bae, Y. H. Kang, C. Lee and S. Y. Cho, *J. Mater. Chem. A*, 2017, **5**, 17867–17873.
51 Z. Li, L. Deng, H. Lv, L. Liang, W. Deng, Y. Zhang and G. Chen, *Adv. Funct. Mater.*, 2021, **31**, 2104836.
52 D. R. Villalva, M. A. Haque, M. I. Nugraha and D. Baran, *ACS Appl. Energy Mater.*, 2020, **3**, 9126–9132.
53 S.-W. Hwang, H. Tao, D.-H. Kim, H. Cheng, J.-K. Song, E. Rill, M. A. Brenckle, B. Panilaitis, S. M. Won, Y.-S. Kim, Y. M. Song, K. J. Yu, A. Ameen, R. Li, Y. Su, M. Yang, D. L. Kaplan, M. R. Zakin, M. J. Slepian, Y. Huang, F. G. Omenetto and J. A. Rogers, *Science*, 2012, **337**, 1640.
54 C. J. Bettinger and Z. Bao, *Adv. Mater.*, 2010, **22**, 651.
55 A. Campana, T. Cramer, D. T. Simon, M. Berggren and F. Biscarini, *Adv. Mater.*, 2014, **26**, 3874.
56 X. Wang, L. Dong, H. Zhang, R. Yu, C. Pan and Z. L. Wang, *Adv. Sci.*, 2015, **2**, 1500169.
57 Y. Y. Lee, H. Y. Kang, S. H. Gwon, G. M. Choi, S. M. Lim, J. Y. Sun and Y. C. Joo, *Adv. Mater.*, 2016, **28**, 1636.
58 S. Mousavi, M. T. Thai, M. Amjadi, D. Howard, S. Peng, T. N. Do and C. H. Wang, *J. Mater. Chem. A*, 2022, **10**, 13673.
59 W. Wang, Z. Li, M. Li, L. Fang, F. Chen, S. Han, L. Lan, J. Chen, Q. Chen, H. Wang, C. Liu, Y. Yang, W. Yue and Z. Xie, *Nano-Micro Lett.*, 2022, **14**, 184.
60 L. Ding, Y. Liu, J. Lai, W. Zhu, C. Fan, N. Hao, J. Wei, J. Qian and K. Wang, *Adv. Funct. Mater.*, 2022, **32**, 2202735.
61 D. He, Y. Zhang, Q. Wu, R. Xu, H. Nan, J. Liu, J. Yao, Z. Wang, S. Yuan, Y. Li, Y. Shi, J. Wang, Z. Ni, L. He, F. Miao, F. Song, H. Xu, K. Watanabe, T. Taniguchi, J.-B. Xu and X. Wang, *Nat. Commun.*, 2014, **5**, 5162.
62 Y. Kim, H. Noh, B. D. Paulsen, J. Kim, I.-Y. Jo, H. Ahn, J. Rivnay and M.-H. Yoon, *Adv. Mater.*, 2021, **33**, 2007550.
63 C. Z. Liao, C. H. Mak, M. Zhang, H. L. Chan and F. Yan, *Adv. Mater.*, 2015, **27**, 676.
64 M. L. Hammock, O. Knopfmacher, T. N. Ng, J. B. Tok and Z. Bao, *Adv. Mater.*, 2014, **26**, 6138.
65 X. Su, X. Wu, S. Chen, A. M. Nedumaran, M. Stephen, K. Hou, B. Czarny and W. L. Leong, *Adv. Mater.*, 2022, **34**, 2200682.
66 J. Ouyang, Q. Xu, C. W. Chu, Y. Yang, G. Li and J. Shinar, *Polymer*, 2004, **45**(25), 8443–8450.
67 J. Ouyang, C. W. Chu, C. R. Szmanda, L. Ma and Y. Yang, *Nat. Mater.*, 2004, **3**(12), 918–922.
68 J. Ouyang, C. W. Chu, F. C. Chen, Q. Xu and Y. Yang, *Adv. Funct. Mater.*, 2005, **15**(2), 203–208.
69 Y. Xia and J. Ouyang, *Macromolecules*, 2009, **42**(12), 4141–4147.
70 Y. Xia and J. Ouyang, *J. Mater. Chem.*, 2011, **21**(13), 4927–4936.
71 J. Ouyang, *Displays*, 2013, **34**(5), 423–436.
72 Y. Xia, K. Sun and J. Ouyang, *Energy Environ. Sci.*, 2012, **5**(1), 5325–5332.
73 Y. Xia, K. Sun and J. Ouyang, *Adv. Mater.*, 2012, **24**, 2436.
74 K. Sun, Y. Xia and J. Ouyang, *Sol. Energy Mater. Sol. Cells*, 2012, **97**, 89–96.
75 J. Ouyang, *ACS Appl. Mater. Interfaces*, 2013, **5**, 13082.
76 Y. Xia and J. Ouyang, *ACS Appl. Mater. Interfaces*, 2013, **2**(2), 474–483.
77 Y. Xia, K. Sun, J. Chang and J. Ouyang, *J. Mater. Chem. A*, 2015, **3**(31), 15897–15904.
78 P. Li, K. Sun and J. Ouyang, *ACS Appl. Mater. Interfaces*, 2015, **7**, 18415.
79 K. Sun, P. Li, Y. Xia, J. Chang and J. Ouyang, *ACS Appl. Mater. Interfaces*, 2015, **7**, 15314.
80 Y. Xia, J. Fang, P. Li, B. Zhang, H. Yao, J. Chen, J. Ding and J. Ouyang, *ACS Appl. Mater. Interfaces*, 2017, **9**, 19001.
81 F. Wu, P. Li, K. Sun, Y. Zhou, W. Chen, J. Fu, M. Li, S. Lu, D. Wei, X. Tang, Z. Zang, L. Sun, X. Liu and J. Ouyang, *Adv. Electron. Mater.*, 2017, **3**, 1700047.
82 B. C. K. Tee and J. Ouyang, *Adv. Mater.*, 2018, **30**(47), 1802560.
83 R. Chen, H. He, X. Hong, Q. Le, K. Sun and J. Ouyang, *Macromolecules*, 2022, **55**(12), 4967–4978.
84 Y. Fang, H. Cheng, H. He, S. Wang, J. Li, S. Yue, L. Zhang, Z. Du and J. Ouyang, *Adv. Funct. Mater.*, 2020, **30**(51), 2004699.
85 S. Wang, Y. Fang, H. He, L. Zhang, C. Li and J. Ouyang, *Adv. Funct. Mater.*, 2020, **31**(5), 2007495.
86 L. Zhang, J. Li, S. Yue, H. He and J. Ouyang, *Adv. Funct. Mater.*, 2021, **31**(30), 2102745.
87 X. Guan and J. Ouyang, *CCS Chem.*, 2021, **3**(10), 2415–2427.
88 S. Wang, Y. Fang, H. He, L. Zhang, C. Li and J. Ouyang, *Adv. Funct. Mater.*, 2021, **31**(5), 2007495.
89 Z. Liu, H. Cheng, H. He, J. Li and J. Ouyang, *Adv. Funct. Mater.*, 2022, **32**(7), 2109772.
90 Z. Liu, H. Cheng, Q. Le, R. Chen, J. Li and J. Ouyang, *Adv. Energy Mater.*, 2022, **12**(22), 2200858.
91 Y. F. Li, X. Fan, C. Shen, X. Shi, P. C. Li, K. Hui, J. P. Fan, K. Kang, T. Zhang and L. Qian, *Adv. Funct. Mater.*, 2022, **32**, 2203641.
92 Y. F. Li, R. J. Wen, P. C. Li and X. Fan, *ACS Appl. Energy Mater.*, 2022, **5**(6), 7692.
93 X. Fan, *Adv. Funct. Mater.*, 2021, **31**, 2009399.
94 J. Wan, Y. Xia, B. Xu, J. Fang, Z. Zhang, J. Wang, X. Fan and Y. Li, *Nano-Micro Lett.*, 2021, **13**, 44.
95 J. Wan, R. Wen, Y. Xia, M. Dai, H. Huang, L. Xue, Z. Zhang, J. F. Fang, K. N. Hui and X. Fan, *J. Mater. Chem. A*, 2021, **9**, 5425.
96 J. Wan, X. Fan, Y. Li, P. Li, T. Zhang, K. Hui, H. Huang, K. Kang and L. Qian, *Front. Chem.*, 2022, **9**, 807538.
97 R. J. Wen, H. H. Huang, J. Y. Wan, S. C. Wen, J. Z. Wang and X. Fan, *Energy Technol.*, 2021, 2100595.

98 X. Fan, R. J. Wen, Y. G. Xia, J. Z. Wang, X. H. Liu, H. H. Huang, Y. Li, W. Y. Zhu, Y. J. Cheng, L. J. Ma, J. F. Fang, H. Tsai and W. Y. Nie, *Sol. RRL*, 2020, **4**, 1900543.
99 J. Wan, X. Fan, H. Huang, J. Wang, Z. Zhang, J. Fang and F. Yan, *J. Mater. Chem. A*, 2020, **8**(40), 21007–21015.
100 X. Fan, W. Y. Nie, H. Tsai, N. X. Wang, H. H. Huang, Y. J. Cheng, R. J. Wen, L. J. Ma, F. Yan and Y. G. Xia, *Adv. Sci.*, 2019, **6**, 1900813.
101 X. Fan, W. Song, T. Lei, B. Xu, F. Yan, N. Wang, H. Cui and Z. Ge, *Mater. Chem. Front.*, 2019, **3**, 901.
102 W. Song, X. Fan, B. Xu, F. Yan, H. Cui, Q. Wei, R. Peng, L. Hong, J. Huang and Z. Ge, *Adv. Mater.*, 2018, **30**, 1800075.
103 X. Fan, N. Wang, J. Wang, B. Xu and F. Yan, *Mater. Chem. Front.*, 2018, **2**, 355.
104 X. Fan, N. Wang, F. Yan, J. Wang, W. Song and Z. Ge, *Adv. Mater. Technol.*, 2018, **3**, 1800030.
105 X. Fan, B. Xu, N. X. Wang, J. Z. Wang, S. H. Liu, H. Wang and F. Yan, *Adv. Electron. Mater.*, 2017, **3**, 1600471.
106 X. Fan, B. Xu, S. Liu, C. Cui, J. Wang and F. Yan, *ACS Appl. Mater. Interfaces*, 2016, **8**, 14029.
107 X. Fan, J. Z. Wang, H. B. Wang, X. Liu and H. Wang, *ACS Appl. Mater. Interfaces*, 2015, **7**, 16287.
108 X. Fan, J. Wang, H. Huang and H. Wang, *ACS Photonics*, 2014, **1**, 1278–1284.
109 X. Fan, S. Guo, G. Fang, C. Zhan, H. Wang, Z. Zhang and Y. Li, *Sol. Energy Mater. Sol. Cells*, 2013, **113**, 135–139.
110 X. Fan, C. Cui, G. Fang, J. Wang, S. Li, F. Cheng, H. Long and Y. Li, *Adv. Funct. Mater.*, 2012, **22**, 585.
111 M. N. Gueyea, A. Carellaa, J. Faure-Vincentc, R. Demadrillec and J.-P. Simonato, *Prog. Mater. Sci.*, 2020, **108**, 100616.
112 Y. Y. Jiang, T. F. Liu and Y. H. Zhou, *Adv. Funct. Mater.*, 2020, **30**, 2006213.
113 L. V. Kayser and D. J. Lipomi, *Adv. Mater.*, 2019, **31**, 1806133.
114 J. S. Park, G.-U. Kim, S. Lee, J. Woo Lee, S. Li, J.-Y. Lee and B. J. Kim, *Adv. Mater.*, 2022, **34**, 2201623.
115 S. Wanga, G. Zuo, J. Kim and H. Sirringhaus, *Prog. Polym. Sci.*, 2022, **129**, 101548.
116 Y. Yang, H. Deng and Q. Fu, *Mater. Chem. Front.*, 2020, **4**, 3130–3152.
117 Y. Hao, X. He, L. Wang, X. Qin, G. Chen and J. Yu, *Adv. Funct. Mater.*, 2022, **32**, 2109790.
118 G. L. Ong, T. S. Ong, S. L. Yap, D.-J. Liaw, T. Y. Tou, S. S. Yap and C. H. Nee, *Nanotechnol. Rev.*, 2022, **11**, 1870–1889.
119 C. Nguyen-Trung, D. A. Palmer, G. M. Begun, C. Peifert and R. E. Mesmer, *J. Solution Chem.*, 2000, **29**, 101–129.
120 S. Garreau, G. Louarn, J. P. Buisson, G. Froyer and S. Lefrant, *Macromolecules*, 1999, **32**, 6807–6812.
121 C. G. Granqvist, *Sol. Energy Mater. Sol. Cells*, 2007, **91**, 1529.
122 D. A. Waldow, M. D. Ediger, Y. Yamaguchi, Y. Matsushita and I. Noda, *Macromolecules*, 1991, **24**, 3147.
123 A. C. Hinckley, S. C. Andrews, M. T. Dunham, A. Sood, M. T. Barako, S. Schneider, M. F. Toney, K. E. Goodson and Z. N. Bao, *Adv. Electron. Mater.*, 2021, **7**, 2001190.
124 Q. Wei, M. Mukaida, Y. Naitoh and T. Ishida, *Adv. Mater.*, 2013, **25**, 2831.
125 C. Badre, L. Marquant, A. M. Alsayed and L. A. Hough, *Adv. Funct. Mater.*, 2012, **22**, 2723.
126 X. Li, W. Zhang, X. Guo, C. Lu, J. Wei and J. Fang, *Science*, 2022, **375**, 434.
127 J. Park, J. Kim, H.-S. Yun, M. J. Paik, E. Noh, H. J. Mun, M. G. Kim, T. J. Shin and S. I. Seok, *Nature*, 2023, **616**, 724–730.
128 C. Duan, Z. Liu, L. Yuan, H. Zhu, H. Luo and K. Yan, *Adv. Opt. Mater.*, 2020, **8**, 2000216.
129 F. Wu, K. R. Yan, H. T. Wu, B. F. Niu, Z. X. Liu, Y. K. Li, L. J. Zuo and H. Z. Chen, *J. Mater. Chem. A*, 2021, **9**, 14920–14927.
130 C. T. Zuo and L. M. Ding, *Adv. Energy Mater.*, 2017, **7**, 1601193.
131 W. Li, H. X. Wang, X. F. Hu, W. S. Cai, C. Zhang, M. Wang and Z. G. Zang, *Sol. RRL*, 2021, **5**, 2000573.
132 L. Hu, K. Sun, M. Wang, W. Chen, B. Yang, J. Fu, Z. Xiong, X. Li, X. Tang, Z. Zang, S. Zhang, L. Sun and M. Li, *ACS Appl. Mater. Interfaces*, 2017, **9**, 43902–43909.
133 K. Jiang, F. Wu, G. Y. Zhang, P. C. Y. Chow, C. Ma, S. F. Li, K. S. Wong, L. Zhu and H. Yan, *J. Mater. Chem. A*, 2019, **7**, 21662–21667.
134 W. Hu, C. Xu, L. Niu, A. Elseman, G. Wang, D. Liu, Y. Yao, L. Liao, G. Zhou and Q. Song, *ACS Appl. Mater. Interfaces*, 2019, **11**, 22021–22027.
135 D. Y. Liu, Y. Li, J. Y. Yuan, Q. M. Hong, G. Z. Shi, D. Yuan, J. Wei, C. C. Huang, J. Tang and M. K. Fung, *J. Mater. Chem. A*, 2017, **5**, 5701–5708.
136 K. Chen, Q. Hu, T. Liu, L. Zhao, D. Luo, J. Wu, Y. Zhang, W. Zhang, F. Liu, T. Russell, R. Zhu and Q. Gong, *Adv. Mater.*, 2016, **28**, 10718–10724.
137 N. Kim, B. H. Lee, D. Choi, G. Kim, H. Kim, J.-R. Kim, J. Lee, Y. H. Kahng and K. Lee, *Phys. Rev. Lett.*, 2012, **109**, 106405.
138 X. Y. Zhou, M. M. Hu, C. Liu, L. Z. Zhang, X. W. Zhong, X. N. Li, Y. Q. Tian, C. Cheng and B. M. Xu, *Nano Energy*, 2019, **63**, 103866.
139 H. Elbohy, B. Bahrami, S. Mabrouk, K. M. Reza, A. Gurung, R. Pathak, M. Liang, Q. Q. Qiao and K. Zhu, *Adv. Funct. Mater.*, 2019, **29**, 1806740.
140 J. Yoon, H. Sung, G. Lee, W. Cho, N. Ahn, H. S. Jung and M. Choi, *Energy Environ. Sci.*, 2017, **10**, 337.
141 L. G. Xu, M. Y. Qian, C. Zhang, W. Z. Lv, J. B. Jin, J. S. Zhang, C. Zheng, M. G. Li, R. F. Chen and W. Huang, *Nano Energy*, 2020, **67**, 104244.
142 M. Wang, H. X. Wang, W. Li, X. F. Hu, K. Sun and Z. G. Zang, *J. Mater. Chem. A*, 2019, **7**(46), 26421.
143 S. Ma, X. Liu, Y. Wu, Y. Tao, Y. Ding, M. Cai, S. Dai, X. Liu, A. Alsaedi and T. Hayat, *Sol. Energy Mater. Sol. Cells*, 2020, **208**, 110379.
144 S. D. Stranks, G. E. Eperon, G. Grancini, C. Menelaou, M. J. P. Alcocer, T. Leijtens, L. M. Herz, A. Petrozza and H. J. Snaith, *Science*, 2013, **342**, 341–344.
145 D. Shi, V. Adinolfi, R. Comin, M. Yuan, E. Alarousu, A. Buin, Y. Chen, S. Hoogland, A. Rothenberger and K. Katsiev, *Science*, 2015, **347**, 519–522.
146 Q. Dong, Y. Fang, Y. Shao, P. Mulligan, J. Qiu, L. Cao and J. Huang, *Science*, 2015, **347**, 967–970.

147 X. Hu, X. D. Zhang, L. Liang, J. Bao, S. Li, W. L. Yang and Y. Xie, *Adv. Funct. Mater.*, 2014, **24**, 7373–7380.
148 H. R. Xia, J. Li, W. T. Sun and L. M. Peng, *Chem. Commun.*, 2014, **50**, 13695–13697.
149 Y. J. Fang, Q. F. Dong, Y. C. Shao, Y. B. Yuan and J. S. Huang, *Nat. Photonics*, 2015, **9**, 679–686.
150 Q. Q. Lin, A. Armin, P. L. Burn and P. Meredith, *Nat. Photonics*, 2015, **9**, 687–694.
151 C. Xie, P. You, Z. Liu, L. Li and F. Yan, *Light: Sci. Appl.*, 2017, **6**(8), e17023.
152 L. Zheng, T. Zhu, W. Xu, L. Liu, J. Zheng, X. Gong and F. Wudl, *J. Mater. Chem. C*, 2018, **6**, 3634.
153 L. Dou, Y. M. Yang, J. You, Z. Hong, W.-H. Chang, G. Li and Y. Yang, *Nat. Commun.*, 2014, **5**, 5404.
154 S. A. McDonald, G. Konstantatos, S. Zhang, P. W. Cyr, E. J. Klem, L. Levina and E. H. Sargent, *Nat. Mater.*, 2005, **4**, 138.
155 T. Zhu, L. Zheng, X. Yao, L. Liu, F. Huang, Y. Cao and X. Gong, *ACS Appl. Mater. Interfaces*, 2019, **11**, 9205.
156 X. Xu, C. C. Chueh, P. Jing, Z. Yang, X. Shi, T. Zhao, L. Y. Lin and A. K. Y. Jen, *Adv. Funct. Mater.*, 2017, **27**, 1701053.
157 C. K. Liu, Q. Tai, N. Wang, G. Tang, Z. Hu and F. Yan, *ACS Appl. Mater. Interfaces*, 2020, **12**(16), 18769–18776.
158 J. Y. Li, Z. Y. Han, Y. Gu, D. J. Yu, J. X. Liu, D. W. Hu, X. B. Xu and H. B. Zeng, *Adv. Funct. Mater.*, 2021, **31**, 2008684.
159 H. Wei, Y. Fang, P. Mulligan, W. Chuirazzi, H.-H. Fang, C. Wang, B. R. Ecker, Y. Gao, M. A. Loi, L. Cao and J. Huang, *Nat. Photonics*, 2016, **10**, 333.
160 S. Yakunin, M. Sytnyk, D. Kriegner, S. Shrestha, M. Richter, G. J. Matt, H. Azimi, C. J. Brabec, J. Stangl, M. V. Kovalenko and W. Heiss, *Nat. Photonics*, 2015, **9**, 444.
161 Z. Chen, Q. Dong, Y. Liu, C. Bao, Y. Fang, Y. Lin, S. Tang, Q. Wang, X. Xiao, Y. Bai, Y. Deng and J. Huang, *Nat. Commun.*, 2017, **8**, 1890.
162 R. Guo, C. Bao, F. Gao and J. Tian, *Adv. Opt. Mater.*, 2020, **8**, 2000557.
163 R. Guo, F. Huang, K. Zheng, T. Pullerits and J. Tian, *ACS Appl. Mater. Interfaces*, 2018, **10**, 35656–35663.
164 W. Hu, W. Huang, S. Yang, X. Wang, Z. Jiang, X. Zhu, H. Zhou, H. Liu, Q. Zhang and X. Zhuang, *Adv. Mater.*, 2017, **29**, 1703256.
165 T. Zhu, Y. Yang, L. Zheng, L. Liu, M. L. Becker and X. Gong, *Adv. Funct. Mater.*, 2020, **30**, 1909487.
166 Z. Fan and J. Ouyang, *Adv. Electron. Mater.*, 2019, **5**, 1800769.
167 H. Yao, Z. Fan, H. Cheng, X. Guan, C. Wang, K. Sun and J. Ouyang, *Macromol. Rapid Commun.*, 2018, 1700727.
168 Z. Fan, D. Du, Z. Yu, P. Li, Y. Xia and J. Ouyang, *ACS Appl. Mater. Interfaces*, 2016, **8**, 23204–23211.
169 S. Zhang, Z. Fan, X. Wang, Z. Zhang and J. Ouyang, *J. Mater. Chem. A*, 2018, **6**, 7080–7087.
170 Z. Fan, P. Li, D. Du and J. Ouyang, *Adv. Energy Mater.*, 2017, **7**, 1602116.
171 O. Bubnova, Z. U. Khan, A. Malti, S. Braun, M. Fahlman, M. Berggren and X. Crispin, *Nat. Mater.*, 2011, **10**, 429–433.
172 S. Yue, H. Cheng, H. He, X. Guan, Q. Le, X. Shu, S. Shi, J. Chen and J. Ouyang, *J. Mater. Chem. A*, 2021, **9**, 16725.
173 B. Li, S. Yue, H. Cheng, C. Wu and J. Ouyang, *J. Mater. Chem. A*, 2022, **10**, 862–871.
174 W. S. Kim, G. Anoop, I. S. Jeong, H. J. Lee, H. B. Kim, S. H. Kim, G. W. Goo, H. Lee, H. J. Lee, C. Kim, J. H. Lee, B. S. Mun, J. W. Park, E. Lee and J. Y. Jo, *Nano Energy*, 2020, **67**, 104207.
175 G. P. Moriarty, S. De, P. J. King, U. Khan, M. Via, J. A. King, J. N. Coleman and J. C. Grunlan, *J. Polym. Sci., Part B: Polym. Phys.*, 2013, **51**, 119.
176 J.-H. Hsu, W. Choi, G. Yang and C. Yu, *Org. Electron.*, 2017, **45**, 182.
177 S. Liu, H. Li and C. He, *Carbon*, 2019, **149**, 25–32.
178 C. Li, X. Guan, S. Yue, X. Z. Wang, J. Li, H. Cheng, S. Wang, A. K. K. Kyaw and J. Ouyang, *J. Mater. Chem. A*, 2021, **9**, 16952.
179 X. Guan, W. Feng, X. Wang, R. Venkatesh and J. Ouyang, *ACS Appl. Mater. Interfaces*, 2020, **12**, 13013–13020.
180 X. Guan, E. Yildirim, Z. Fan, W. Lu, B. Li, K. Zeng, S. W. Yang and J. Ouyang, *J. Mater. Chem. A*, 2020, **8**, 13600–13609.
181 D. Zhao, H. Wang, Z. U. Khan, J. C. Chen, R. Gabrielsson, M. P. Jonsson, M. Berggren and X. Crispin, *Energy Environ. Sci.*, 2016, **9**, 1450–1457.
182 Z. Fan, D. Du, X. Guan and J. Ouyang, *Nano Energy*, 2018, **51**, 481.
183 H. Cheng and J. Ouyang, *Adv. Energy Mater.*, 2020, **10**, 2001633.
184 X. Guan, H. Cheng and J. Ouyang, *J. Mater. Chem. A*, 2018, **6**, 19347–19352.
185 S. Wagner and S. Bauer, *MRS Bull.*, 2012, **37**, 207.
186 X. Hu, P. Krull, B. de Graff, K. Dowling, J. A. Rogers and W. J. Arora, *Adv. Mater.*, 2011, **23**, 2933.
187 T. Sekitani, Y. Noguchi, K. Hata, T. Fukushima, T. Aida and T. Someya, *Science*, 2008, **321**, 1468.
188 Z. Liu, S. Fang, F. Moura, J. Ding, N. Jiang, J. Di, M. Zhang, X. Lepro, D. Galvao, C. Haines, N. Yuan, S. Yin, D. Lee, R. Wang, H. Y. Wang, W. Lv, C. Dong, R. Zhang, M. Chen, Q. Yin, Y. Chong, R. Zhang, X. Wang, M. Lima, R. Ovalle-Robles, D. Qian, H. Lu and R. H. Baughman, *Science*, 2015, **349**, 400.
189 Z. Y. Liu, D. P. Qi, P. Z. Guo, Y. Liu, B. W. Zhu, H. Yang, Y. Q. Liu, B. Li, C. G. Zhang, J. C. Yu, B. Liedberg and X. D. Chen, *Adv. Mater.*, 2015, **27**, 6230.
190 Z. Shen, Z. Zhang, N. Zhang, J. Li, P. Zhou, F. Hu, Y. Rong, B. Lu and G. Gu, *Adv. Mater.*, 2022, **34**, 2203650.
191 D. McCoul, W. Hu, M. Gao, V. Mehta and Q. Pei, *Adv. Electron. Mater.*, 2016, **2**, 1500407.
192 M. Zhang, C. Wang, H. Wang, M. Jian, X. Hao and Y. Zhang, *Adv. Funct. Mater.*, 2017, **27**, 1604795.
193 G. Shen, B. Chen, T. Liang, Z. Liu, S. Zhao, J. Liu, C. Zhang, W. Yang, Y. Wang and X. He, *Adv. Electron. Mater.*, 2020, **6**, 1901360.
194 S. Xu, Z. Fan, S. Yang, X. Zuo, Y. Guo, H. Chen and L. Pan, *ACS Sens.*, 2021, **6**, 1120–1128.
195 D. J. Lipomi, B. C. K. Tee, M. Vosgueritchian and Z. Bao, *Adv. Mater.*, 2011, **23**, 1771.

196 M. Kaltenbrunner, M. S. White, E. D. Glowacki, T. Sekitani, T. Someya, N. S. Sariciftci and S. Bauer, *Nat. Commun.*, 2012, **3**, 770.
197 M. Kaltenbrunner, G. Adam, E. D. Głowacki, M. Drack, R. Schwödiauer, L. Leonat, D. H. Apaydin, H. Groiss, M. C. Scharber, M. S. White, N. S. Sariciftci and S. Bauer, *Nat. Mater.*, 2015, **14**, 1032.
198 C.-P. Chen, C.-Y. Chiang, Y. Y. Yu, Y.-S. Hsiao and W.-C. Chen, *Sol. Energy Mater. Sol. Cells*, 2017, **165**, 111–118.
199 J.-W. Lee, G.-U. Kim, D. J. Kim, Y. Jeon, S. Li, T.-S. Kim, J.-Y. Lee and B. J. Kim, *Adv. Energy Mater.*, 2022, **12**, 2200887.
200 J. Wang, C. Han, F. Bi, D. Huang, Y. Wu, Y. Li, S. Wen, L. Han, C. Yang, X. Bao and J. Chu, *Energy Environ. Sci.*, 2021, **14**, 5968–5978.
201 C. Xie, X. Jiang, Q. Zhu, D. Wang, C. Xiao, C. Liu, W. Ma, Q. Chen and W. Li, *Small Methods*, 2021, 2100481.
202 C. Xie, C. Xiao, X. Jiang, S. Liang, C. Liu, Z. Zhang, Q. Chen and W. Li, *Macromolecules*, 2022, **55**, 322–330.
203 J. H. Kim and J. W. Park, *Sci. Adv.*, 2021, **7**, eabd9715.
204 C. Larson, B. Peele, S. Li, S. Robinson, M. Totaro, L. Beccai, B. Mazzolai and R. Shepherd, *Science*, 2016, **351**, 1071.
205 J. Liang, L. Li, X. Niu, Z. Yu and Q. Pei, *Nat. Photonics*, 2013, **7**, 817–824.
206 Z. Yu, X. Niu, Z. Liu and Q. Pei, *Adv. Mater.*, 2011, **23**, 3989.
207 T. Sekitani, H. Nakajima, H. Maeda, T. Fukushima, T. Aida, K. Hata and T. Someya, *Nat. Mater.*, 2009, **8**, 494.
208 J. Xu, S. Wang, G.-J. N. Wang, C. Zhu, S. Luo, L. Jin, X. Gu, S. Chen, V. R. Feig, J. W. F. To, S. Rondeau-Gagné, J. Park, B. C. Schroeder, C. Lu, J. Y. Oh, Y. Wang, Y.-H. Kim, H. Yan, R. Sinclair, D. Zhou, G. Xue, B. Murmann, C. Linder, W. Cai, J. B.-H. Tok, J. W. Chung and Z. Bao, *Science*, 2017, **355**, 59.
209 Y. Q. Zheng, Y. Liu, D. Zhong, S. Nikzad, S. Liu, Z. Yu, D. Liu, H. C. Wu, C. Zhu, J. Li, H. Tran, J. B. Tok and Z. Bao, *Science*, 2021, **373**, 88.
210 Z. Zhang, W. Wang, Y. Jiang, Y.-X. Wang, Y. Wu, J.-C. Lai, S. Niu, C. Xu, C.-C. Shih, C. Wang, H. Yan, L. Galuska, N. Prine, H.-C. Wu, D. Zhong, G. Chen, N. Matsuhisa, Y. Zheng, Z. Yu, Y. Wang, R. Dauskardt, X. Gu, J. B. H. Tok and Z. Bao, *Nature*, 2022, **603**, 624.
211 A. Harada, J. Li and M. Kamachi, *Nature*, 1992, **356**, 325–327.
212 Y. Okumura and K. Ito, *Adv. Mater.*, 2001, **13**, 485–487.
213 A. Bin Imran, T. Seki, K. Ito and Y. Takeoka, *Macromolecules*, 2010, **43**, 1975–1980.
214 N. Kim, S. Lienemann, I. Petsagkourakis, D. A. Mengistie, S. Kee, T. Ederth, V. Gueskine, P. Leclere, R. Lazzaroni, X. Crispin and K. Tybrandt, *Nat. Commun.*, 2020, **11**, 1424.
215 Y. J. Jeong, J. Jung, E. H. Suh, D.-J. Yun, J. G. Oh and J. Jang, *Adv. Funct. Mater.*, 2020, **30**, 1905809.
216 J. He and T. M. Tritt, *Science*, 2017, **357**, 6358.
217 R. Mulla and C. W. Dunnill, *ChemSusChem*, 2019, **12**, 3882.
218 Y. Yang, G. Zhao, X. Cheng, H. Deng and Q. Fu, *ACS Appl. Mater. Interfaces*, 2021, **13**, 14599.
219 P. J. Taroni, G. Santagiuliana, K. Wan, P. Calado, M. Qiu, H. Zhang, N. M. Pugno, M. Palma, N. Stingelin-Stutzman, M. Heeney, O. Fenwick, M. Baxendale and E. Bilotti, *Adv. Funct. Mater.*, 2018, **28**, 1704285.
220 N. Wen, Z. Fan, S. Yang, Y. Zhao, C. Li, T. Cong, H. Huang, J. Zhang, X. Guan and L. Pan, *Chem. Eng. J.*, 2021, **426**, 130816.
221 W. Zhao, Z. Wang, Z. Li, L. Shangguan, Z. Chen, C. Li, J. Zhang and Y. Duan, *Appl. Phys. Lett.*, 2021, **118**, 213301.
222 Z. Wang, J. Wang, Z. Li, Z. Chen, L. Shangguan, S. Fan and Y. Duan, *Nano Energy*, 2023, **109**, 108232.